

Exploring PLATO's efficiency in detecting transiting exoplanets around intermediate mass stars.

Jai MIRCHANDANI

Mentor: *Nicholas Jannsen*
Institute of Astronomy, KU Leuven

Supervisor: *Andrew Tkachenko*
Institute of Astronomy, KU Leuven

Master thesis submitted in fulfillment
of the requirements for the degree in
Master of Science in Astronomy and Astrophysics

Academic year 2024-2025

© Copyright by KU Leuven

Without written permission of the promoters and the authors it is forbidden to reproduce or adapt in any form or by any means any part of this publication. Requests for obtaining the right to reproduce or utilize parts of this publication should be addressed to KU Leuven, Faculteit Wetenschappen, Geel Huis, Kasteelpark Arenberg 11 bus 2100, 3001 Leuven (Heverlee), Telephone +32 16 32 14 01. A written permission of the promoter is also required to use the methods, products, schematics and programs described in this work for industrial or commercial use, and for submitting this publication in scientific contests.

Acknowledgements

I thank Dr. Andrew Tkachenko and Nicholas Jannsen for their constant guidance throughout the thesis. Their valuable advice amplified my interest in the topic and significantly boosted my research skills. I want to express my sincere gratitude towards my mother for all the sacrifices that she made to enable me to pursue my higher studies continents away from home. I want to extend my gratitude to my family and Mrs. Connie Duarte for their unconditional support and motivation. Lastly, I would also like to thank all my friends in India and Belgium for keeping me calm throughout my academic journey.

Summary

Context: In the past 3 decades, more than 5700 exoplanets have been discovered through various detection methods. The transit method has emerged as the leading contributor in exoplanet detections. PLAnetary Transits and Oscillations of stars (PLATO) is a space telescope scheduled to launch in 2026 by the European Space Agency (ESA) with a core science goal of detecting transits from earth-like planets around Sun-like stars. Along with its core science goal, PLATO will photometrically monitor thousands of stars for its different complementary science goals. To maximize the efficiency and output of the telescope, a thorough evaluation of mission performance and scope for each science goal must be done before the in-flight operations. For this purpose, an end-to-end simulator for the telescope called PlatoSim has been developed by the Institute of Astronomy at KU Leuven.

Aim: The search for exoplanet transits becomes more and more challenging as the flux of the host star increases. Hence, the understanding of the population of exoplanets around stars more massive than the Sun is limited. In this project, we investigate the performance of PLATO in detecting exoplanets for such challenging cases where the signal strength is very weak. We test the potential of the telescope to detect exoplanets around intermediate-mass stars of different masses. The potential of the telescope to deliver accurate parameters like the planetary radii is also explored. The performance has also been tested for different magnitudes putting the telescope's capabilities under severe scrutiny.

Methods: To attain the aim of this thesis, a parameter space with different configurations of stars, exoplanets, magnitudes, and orbital distances aligned with the study's scientific objectives was selected. For the entire parameter space, end-to-end simulations of PLATO cameras have been carried out by PlatoSim to generate realistic transit light curves by including all the possible natural noise sources. The Transit Least Squares (TLS) algorithm has been implemented for the retrieval of transits from simulated light curves.

Results: The results from the research demonstrate a promising potential of the telescope in detecting exoplanets around stars with mass less than $2 M_{\odot}$. The exoplanet detections were limited to brighter targets for stars with masses exceeding $2 M_{\odot}$. With increasing magnitude, a steep decline in transit occurrence rates for exoplanets smaller than Jupiter was observed. The estimation of radii ratios has a remarkable accuracy for lower magnitude stars but keeps on reducing with increasing magnitude as expected. The overall results of this study indicated an outstanding performance of PLATO for transit detections around intermediate-mass stars with lower magnitude, strongly suggesting their inclusion as potential targets for the telescope although a definitive conclusion requires further evidence based on more challenging cases.

Summary for general audience

Exoplanets or extra-solar planets are defined as planets that orbit around stars other than the Sun. Since the first discovered exoplanets in 1992, more than 5700 exoplanets have been discovered through different detection methods. The most successful method in terms of number of exoplanets discovered is the transit method with more than 4329 exoplanet discoveries. This method detects the change in the host star's brightness with time due to the presence of an exoplanet in our line of sight to the star. Many telescopes operating from ground and space such as Kepler, TESS, and CoRoT are responsible for the success of this method.

To continue this exploration and deepen our understanding of exo-planetary systems, PLAnetary Transits and Oscillations of stars(PLATO) is a space telescope scheduled to launch in 2026 by European Space Agency (ESA) with a core science goal of detecting earth-like planets around Sun-like stars. The telescope won't just be limited to its core science goal, as a large number of stars will be observed by PLATO which will be used to address a variety of science goals. This project tests how well PLATO can detect exoplanets around more massive, and therefore larger, stars, where detection of transits is more challenging due to weaker signals. For this purpose, a simulator called PlatoSim, which can generate the expected data of PLATO has been used. This simulator replicates PLATO's environment by inducing all the noise effects that can affect the quality and strength of the observed signal. The results show PLATO's strong potential in detecting exoplanets around stars which are up to twice as massive as the Sun. Stars bigger than that are detectable only if the exoplanet's size is big and the magnitude of the star is high. For, brighter stars, it is also possible to extract valuable information about the planet like its size with a very high accuracy. However, a definitive conclusion on the feasibility of searching exoplanets around intermediate-mass stars requires further study of more realistic cases.

Contribution statement

The candidate developed an appropriate parameter space for the science goal with the stellar models obtained from Modules for Experiments in Stellar Astrophysics (MESA). PlatoSim was used by the candidate to generate the model light curves corresponding to the parameter space. These model light curves were used by Nicholas Jannsen to create realistic light curves with PlatoSim. All the simulations to generate the realistic light curves were carried out on the supercomputing resources of Vlaams Supercomputer Centrum (VSC). The candidate used the Transit Least Squares (TLS) package for the transit retrieval procedure. The model phase folded light curves were created by the candidate using BAsic Transit Model cAlculatioN in Python (BATMAN) software. The student thanks Nicholas Jannsen and Dr. Andrew Tkachenko for supervising this project.

Acronyms

asPIC all-sky PLATO input catalog.

CoRoT Convection, Rotation and planetary Transits.

DPU Data Processing Unit.

F-CAMs Fast Cameras.

FEE Front end electronics.

FoV Field of View.

FPA Focal Plane Assembly.

FSS FEE support structure.

ICU Instrument Control Unit.

JWST James Webb Space Telescope.

LOP Long Observation Phase.

N-CAMs Normal Cameras.

NSR Noise-to-Signal Ratio.

PLATO PLAnetary Transits and Oscillations of stars.

RV Radial velocity.

SDE Signal Detection efficiency.

SNR Signal to Noise Ratio.

SPR Signal Pollution Ratio.

TESS Transiting Exoplanet Survey Satellite.

TLS Transit Least Squares.

TOU Telescope Optical Unit.

V Visual magnitude.

List of Figures

1.1	Cumulative detection per year by different detection methods. Image courtesy: NASA Exoplanet Archive	2
1.2	Transit method for detection of exoplanets. The image shows the change in star's brightness when a planet obstructs a fraction of the light coming from the star. (Image courtesy: NASA Ames).	3
1.3	Reduced light curve of star TIC 25375553 observed through TESS processed with Lightkurve Collaboration et al. (2018)	4
1.4	Simulated RV of a stellar system with stellar mass $M_{\text{star}} = 1.4M_{\odot}$ and Planet mass $M_p = 1M_{\text{Jup}}$ simulated through exoplanet radial velocity simulator by https://astro.unl.edu . The dots indicate the artificial RV data, the curve indicates the fit and the red line indicates the phase corresponding to the semi-amplitude of the RV curve.	5
1.5	Mass- Period distribution for various exoplanet distribution techniques. Image courtesy: NASA Exoplanet Archive	6
1.6	Left: PLATO multi-camera layout showing the locations of different N-CAM groups and the F-CAMs on the top. Right: Overlap in the field of view by different camera groups showing regions with Number of cameras(n_{cam}) = 6, 12, 18, 24 represented by different shades of Blue. image courtesy: (Jannsen et al., 2024)	8
1.7	a. Noise budget of PLATO at camera level with the effects of Photon, Jitter, and Background noise. b. Noise budget for n-cams $\epsilon \{6,12,18,24\}$ at the instrumental level. Image courtesy: (Jannsen et al., 2024)	10
2.1	Tree diagram visualizing the architecture of PlatoSim software. Image courtesy: (Jannsen et al., 2024)	12
2.2	Left: Stellar radius as a function of stellar mass Right: Variation of effective temperature with stellar mass	14
2.3	Noise budget of PLATO extrapolated upto the magnitude 17 using the PlatoSim. Noise budget for magnitude 8.5 and 16.5 has been highlighted using the green and purple dashed lines respectively.	15
2.4	Variation of the orbital period with stellar mass for 5 fixed orbital distances.	16
2.5	Histograms representing the distribution of orbital parameters for the parameter space. Left: argument of perihelion, right: eccentricity	17
2.6	Comparison of transit retrieval and SDE of K2-110b using the TLS and BLS algorithms. Image courtesy: Hippke, Heller (2019)	19

2.7	SDE statistics for 10,000 synthetic light curves with an injected exoplanet and 10000 synthetic light curves without exoplanet. Left panel: Transit retrieval through BLS algorithm, right panel: transit retrieval through TLS algorithm. Image courtesy: Hippke, Heller (2019)	19
2.8	The reduced χ^2 residuals from BLS(open histogram) and TLS(gray histogram), calculated for 2346 planetary transit light curves from kepler. Image courtesy: Hippke, Heller (2019).	20
2.9	Phase folded light curve of planetary transit around a $1.2 M_\odot$ star simulated from PlatoSim and retrieved through TLS. The blue dots correspond to the simulated data and the red line shows the model of phase folded light curve generated with BATMAN	21
2.10	Phase folded light curve showing quarterly gap in the data	21
2.11	An example periodogram from TLS with highest peak corresponding to 90 days	22
2.12	Simulated light curve from PlatoSim for a $2.2 M_\odot$ star of 12.5 magnitude (grey dots). Light curve of the same system in bins of approximately 1 hour(red dots). Model of the light curve created using BATMAN software (Kreidberg, 2015) (green curve).	22
3.1	Light curves obtained through PlatoSim for Jupiter-like planet around a $1.2 M_\odot$ star. a. Input light curve from PlatoSim b. 8.5 magnitude system c. 10.5 magnitude system d. 12.5 magnitude system e. 14.5 magnitude system f. 16.5 magnitude system	24
3.2	Transit occurrence rate from primary detections for each magnitude bin. This plot excludes the cases that required further analysis due to the presence of quarterly gaps in the data.	25
3.3	Histogram representing periods corresponding to false detections for: a. 8.5 magnitude b. 10.5 magnitude c. 12.5 magnitude d. 14.5 magnitude e. 16.5 magnitude	26
3.4	Transit occurrence rate from primary and secondary detections for each magnitude bin. This plot includes the cases that required further analysis due to the presence of quarterly gaps in the data	27
3.5	The total exoplanet Transit occurrence rate as a function of stellar mass. .	28
3.6	Transit occurrence rate for each magnitude bin.	29
3.7	The correlation matrix representing the transit occurrence rate in each stellar mass and visual magnitude bin.	29
3.8	The correlation matrix representing the transit occurrence rate for each type of exoplanet in all the magnitude bins.	30
3.9	The correlation matrix representing the transit occurrence rate for all the transit depths in each visual magnitude bin.	30
3.10	Transit depth of all TESS objects of interest excluding the known false positives plotted as a function of the apparent magnitude of the host star. Image courtesy: (Winn, 2024)	31
3.11	Radii ratio estimates of all the detected planetary systems (Black dots). The expected linear relation(red dashed line).	32
3.12	Radii ratio estimates plotted separately for 8.5 and 16.5 magnitude bins. The expected linear relation(red dashed line).	34

3.13 Errors in radii ratio estimates for 8.5 and 14.5 magnitude bins.	35
3.14 Mean SPR for all the magnitude bins	36

List of Tables

1.1	Brief overview of all stellar samples from asPIC.	7
2.1	Planetary mass and radius of all the planets injected in the simulations. . .	15
2.2	Selection of range for orbital parameters	16

Contents

Acknowledgements	i
Summary	iii
Summary for general audience	v
Contribution Statement	v
Acronyms	ix
List of Figures	ix
List of Tables	xv
Contents	xvii
1 Introduction	1
1.1 Exoplanet detection methods	1
1.1.1 Transit method for exoplanet detection	2
1.1.2 Radial Velocity	4
1.2 PLATO space telescope	5
1.2.1 Science objectives	6
1.2.2 PLATO image and data acquisition	7
1.2.3 payload	7
1.2.4 PLATO Noise contributors	8
1.3 Focus of this study	9
2 Data: Simulation, processing and Analysis	11
2.1 PlatoSim	11
2.2 Parameter Space	13
2.2.1 Stellar Parameters	13
2.2.2 Planetary parameters	14
2.2.3 Orbital Parameters	14
2.3 Data Analysis	17
2.3.1 Transit retrieval	17

3 Results	23
3.1 Transit occurrence rates	23
3.2 Radii ratios and uncertainties	31
3.3 Effect of SPR	33
4 Conclusions	37
4.1 Future Outlook	37
Bibliography	39
Appendices	45
A Appendix	47

Chapter 1

Introduction

There has been significant growth in the field of extrasolar planets (exoplanets) since the discovery of the first true exoplanets around a pulsar by [Wolszczan, Frail \(1992\)](#). But, the first confirmed exoplanet around a main-sequence star by [Mayor, Queloz \(1995\)](#) is considered to be a big milestone in this field, for which they were awarded a Nobel prize in physics in 2019. On the shoulders of this discovery, our understanding of the solar system and the planet formation models witnessed a paradigm shift in the last 3 decades. Different types of planets and planetary systems were discovered through the evolution of different astronomical techniques, technologies, and detection methods. The normative architecture of the solar system saw the rise of its uniqueness with the discovery of planetary systems with different architectures. For example, the planet detected by [Mayor, Queloz \(1995\)](#) was found to be a Jupiter-like planet orbiting very close to its host star (also called Hot-Jupiters) which is something that is neither seen in our solar system nor predicted in the early models of planetary system formations ([Howell, 2020](#)). Hence, the detection and study of exoplanets have been proven to be beneficial not only for determining the possible mechanisms behind the birth and development of the solar system and our home, Earth but also to understand the existence and formation of planets and life beyond our solar system.

1.1 Exoplanet detection methods

There are various exoplanet detection methods namely Radial velocity (RV), the transit method, direct imaging, pulsar timing, gravitational micro-lensing and astrometry. All these methods have confirmed around 5811 exoplanets ([NASA Exoplanet Archive, 2024](#)) as of December 2024. Each method has different advantages and can provide us with diverse information about the physical, chemical, and dynamic properties of the observed stellar system. The contribution of different detection methods can be seen in Figure 1.1. The discussion below provides detailed insights into the transit method which is the leading contributor in the number of detections as seen in Figure 1.1 and is also the major focus of this thesis. The discussion is followed by a brief description of the RV method as it has emerged to be an essential step for validation of transiting exoplanet candidates. For more information on other detection methods, the reader is referred to the Handbook of exoplanets by ([Deeg, Belmonte, 2018](#)) and exoplanets review by [Seager \(2011\)](#).

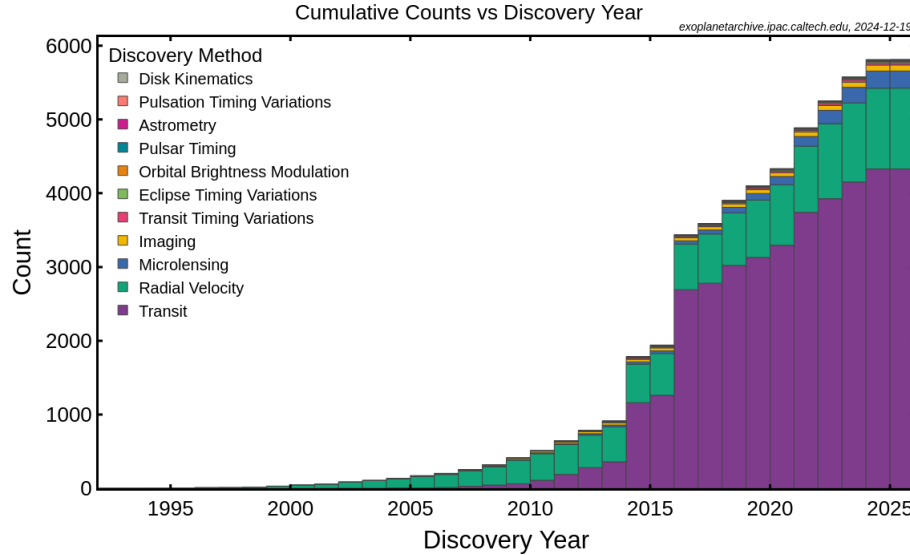


Figure 1.1: Cumulative detection per year by different detection methods. Image courtesy: [NASA Exoplanet Archive](#)

1.1.1 Transit method for exoplanet detection

Investigating the changes in a star's brightness as a function of time has proven to be one of the most effective techniques in various research domains of astronomy and astrophysics. The visual representation of this temporal change of a star's brightness is known as a light curve and it can tell us a lot about the intrinsic properties like pulsations, star-spots and flares as well as extrinsic properties like the presence of another binary companion, exoplanet or accretion disk around the star. An exoplanet at an appropriate inclination with respect to the plane of the sky can cause a temporary dip in brightness of the star by obstructing some of its light, as represented in Figure 1.2 . Such an event is termed as a planetary transit and this method of detecting exoplanets is called the transit method. The first planetary transit was detected around HD 209458 by ([Charbonneau et al., 1999](#)). Since then, many ground-based and space-based missions have been launched dedicated to transit detections, for eg: Kepler ([Borucki et al., 2007](#)) Transiting Exoplanet Survey Satellite (TESS) ([Ricker et al., 2015](#)) and Convection, Rotation and planetary Transits (CoRoT) ([Baglin et al., 2003](#)).

This method of detecting exoplanets has proven to be the most successful in terms of the number of exoplanets detected as also seen in Figure 1.1. As of December 2024, the number of exoplanets discovered through the transit method is 4329, significantly more than the combined number of detected exoplanets from other methods ([NASA Exoplanet Archive, 2024](#)). The high detections from this method doesn't imply a high probability of detecting a transit for a given star because the high detection frequency results from the technological capability of photometrically monitoring many stars in a wide Field of View (FoV). The geometrical probability of detecting an exoplanet is given by ([Winn, 2010](#)) as shown in the equation (1.1).

$$p_{\text{transit}} = \left[\frac{R_{\text{star}} \pm R_{\text{planet}}}{a} \right] \left[\frac{1 + e \sin \omega}{1 - e^2} \right] \quad (1.1)$$

where, p_{transit} is the probability of transit, where, R_{planet} is the radius of the planet, R_{star}

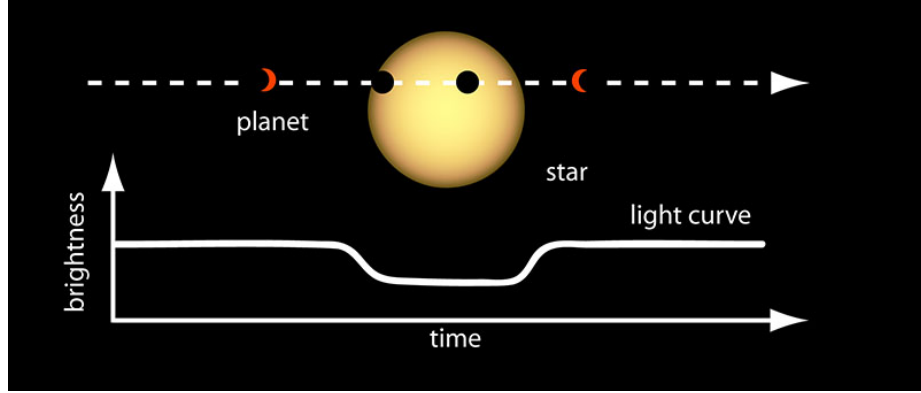


Figure 1.2: Transit method for detection of exoplanets. The image shows the change in star's brightness when a planet obstructs a fraction of the light coming from the star. (Image courtesy: NASA Ames).

is the radius of the star, e is the eccentricity and ω is the argument of perapse. The "+" and "-" in the equation correspond to the minimum inclination required to detect a transit and maximum inclination (90 degrees) respectively.

Apart from the high detection frequency of this method, a light curve showing exoplanet transits is a very useful tool to gain valuable insights about the physical and dynamic properties of the observed star-planet system. To understand the estimation of some parameters, let us consider the light curve shown in Figure 1.3 as an example case. The two dips observed in the flux of star TIC 25375553 are due to two transit occurrences by an exoplanet in its orbit. The time difference between two transits is a direct indication of the period (P) of the exoplanet as it shows the time taken by the planet to return to the same position in its orbit (starting point of the transit) again. In this example, we can see that the period is approximately 2.3 days. Once, the period is estimated, we can use Kepler's 3rd law as shown in the equation (1.2) to estimate the semi-major axis(a).

$$P = \frac{4\pi^2}{GM_{\text{star}}} a^3 \quad (1.2)$$

Another quantity that can be directly measured from the transit observations is transit depth (δ_{transit}) written as:

$$\delta_{\text{transit}} \approx \left[\frac{R_{\text{planet}}}{R_{\text{star}}} \right]^2 \quad (1.3)$$

This equation states that the strength of the observed transit signal is inversely proportional to the stellar radius. As the star gets bigger, it becomes more challenging to detect transiting exoplanets around it.

The evolution of stellar models and RV methods for binary stars have successfully helped us constrain basic stellar parameters such as the mass and radius of the star. This information, hence can further be used to determine the physical and orbital parameters of transiting exoplanets. The transit method has also made the study of exoplanet atmospheres possible through the technique of transit spectroscopy first presented by ([Bundy, Marcy, 2000](#)). In this technique, the spectroscopic data of the star is obtained when an exoplanet is transiting it. By comparing this data to the same star during non-transit

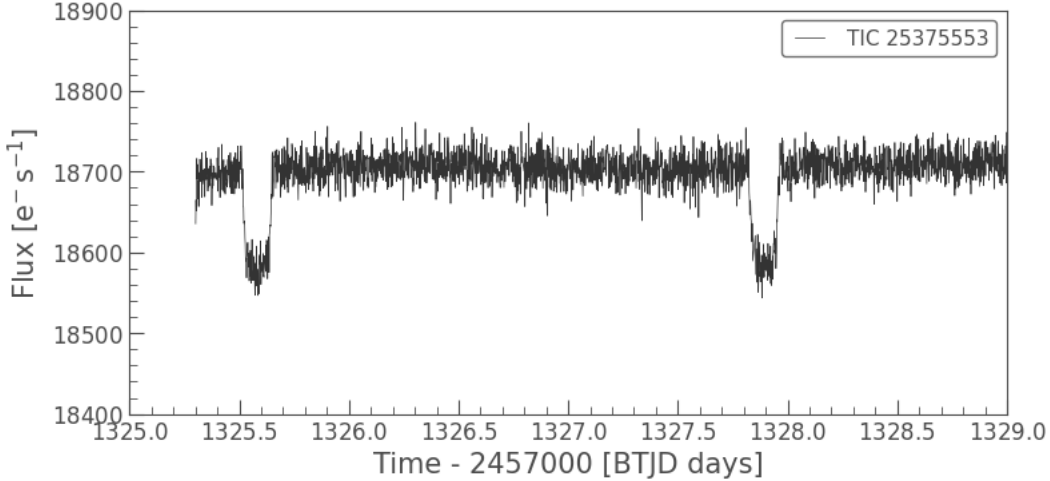


Figure 1.3: Reduced light curve of star TIC 25375553 observed through TESS processed with [Lightkurve Collaboration et al. \(2018\)](#)

time or a similar star of the same spectral class, the emission or absorption lines from the molecules present in the transiting exoplanet atmospheres can be identified ([Lee, 2018](#)). This study is very useful to understand the habitability of exoplanets. The detection of life-forming molecules or so-called bio-signature molecules, like CO_2 , N_2 in the habitable zone of the star is currently the leading way to look out for life beyond the solar system.

1.1.2 Radial Velocity

A limitation of the transit method is that the transit signal obtained from a star can sometimes be mimicked by other stellar effects leading to the introduction of false positives in the data. Hence The evolution of the transit method has pushed the RV method as a follow-up procedure for confirming the transiting exoplanet candidates ([Deeg, Alonso, 2018](#)).

The technological developments in spectrographs ([Cenadelli, Bernagozzi, 2018](#)), coupled with significant improvements in stabilization and calibration by [Latham et al. \(1988\)](#), led to the eventual discovery of the first confirmed exoplanet around a main sequence star using the RV method in 1995. The common notion that a planet revolves around a star is not entirely accurate, as both the planet and the star revolve around a center of mass, which typically lies inside the star (though not precisely at its center), causing the star to wobble along our line of sight ([Wright, Gaudi, 2013](#)). This wobble can manifest as a doppler shift in the spectroscopic signal of the star, indicating the presence of exoplanet(s) around the star. From the observed doppler shift, we can deduce the velocities of the star along our line of sight, also referred to as the radial velocity of the star ([Lindegren, Lennart, Dravins, Dainis, 2003](#)). The change in radial velocity as a function of time/phase, also known as the RV curve illustrated in Figure 1.4 is a sinusoidal curve that provides us with an estimate of various stellar and planetary parameters within the observed system. The semi amplitude of this RV curve can be written as:

$$K = \left(\frac{2\pi G}{P} \right)^{1/3} \frac{M_p \sin i}{(M_{\text{star}} + M_p)^{2/3}} \frac{1}{\sqrt{1 - e^2}} \quad (1.4)$$

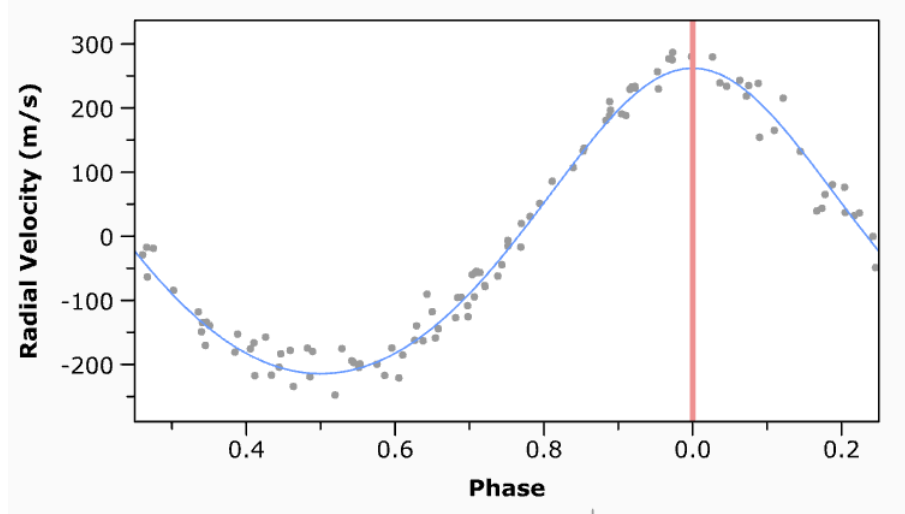


Figure 1.4: Simulated RV of a stellar system with stellar mass $M_{\text{star}} = 1.4M_{\odot}$ and Planet mass $M_p = 1M_{\text{Jup}}$ simulated through exoplanet radial velocity simulator by <https://astro.unl.edu>. The dots indicate the artificial RV data, the curve indicates the fit and the red line indicates the phase corresponding to the semi-amplitude of the RV curve.

Where, M_p is the mass of the planet, M_{star} is the mass of the star, i is the inclination of the orbit with respect to the plane of sky and P is the period of the detected exoplanet. For a system with known stellar mass, the semi amplitude of this RV curve can constrain the upper bounds for the mass of the planet ($M_p \sin i$). Currently, there are 1090 planets discovered through this method ([NASA Exoplanet Archive, 2024](#)).

1.2 PLATO space telescope

Observing transiting exoplanets requires high precision because of which the detections from ground-based telescopes are restricted to higher mass exoplanets ([Lee, 2018](#)). Hence, this has boosted the need to go to space where the loss of signal due to atmospheric effects like turbulence is negligible when compared to on-ground observations. As a result, Kepler and its extension K2, TESS and CoRoT are among those groundbreaking telescopes responsible for the detection of majority of transiting exoplanets.

It can be seen from Figure 1.5 that the frequency of detected exoplanets reduces for higher periods. Hence, the progress in detection of exoplanets with periods similar to Earth (365 days) is still comparatively less. The study of Terrestrial (earth-like) planets at an appropriate distance around the host star is essential to understanding the existence of habitable exoplanets. The study of planets in the habitable zone where liquid water can exist is one of the very few techniques capable of giving us insights on existence of life beyond our solar system. Detection and estimation of bulk properties of such exoplanets also open up doors for the study of their atmospheres through transit spectroscopy. Looking for an Earth-like planet around Sun-like star is a stepping stone towards understanding the habitable systems but past and present telescopes have been vastly unsuccessful in detecting Earth-Sun analogs.

Hence, a new space telescope by ESA named PLAnetary Transits and Oscillations of

stars (PLATO) (Rauer et al., 2024) is planned to be launched in 2026 with a core science goal of studying earth-like planets in the habitable zone of Sun-like stars through transit photometry. Similar to James Webb Space Telescope (JWST) launched in 2021, PLATO will operate 1.5 million km away from Earth at the second Lagrange point (L2). PLATO will have targets in 2 Long Observation Phase (LOP) fields of at least 2 years each so that at least 2 transits can be detected from the exoplanets having orbital periods as long as approximately a year (Montalto, M. et al., 2021).

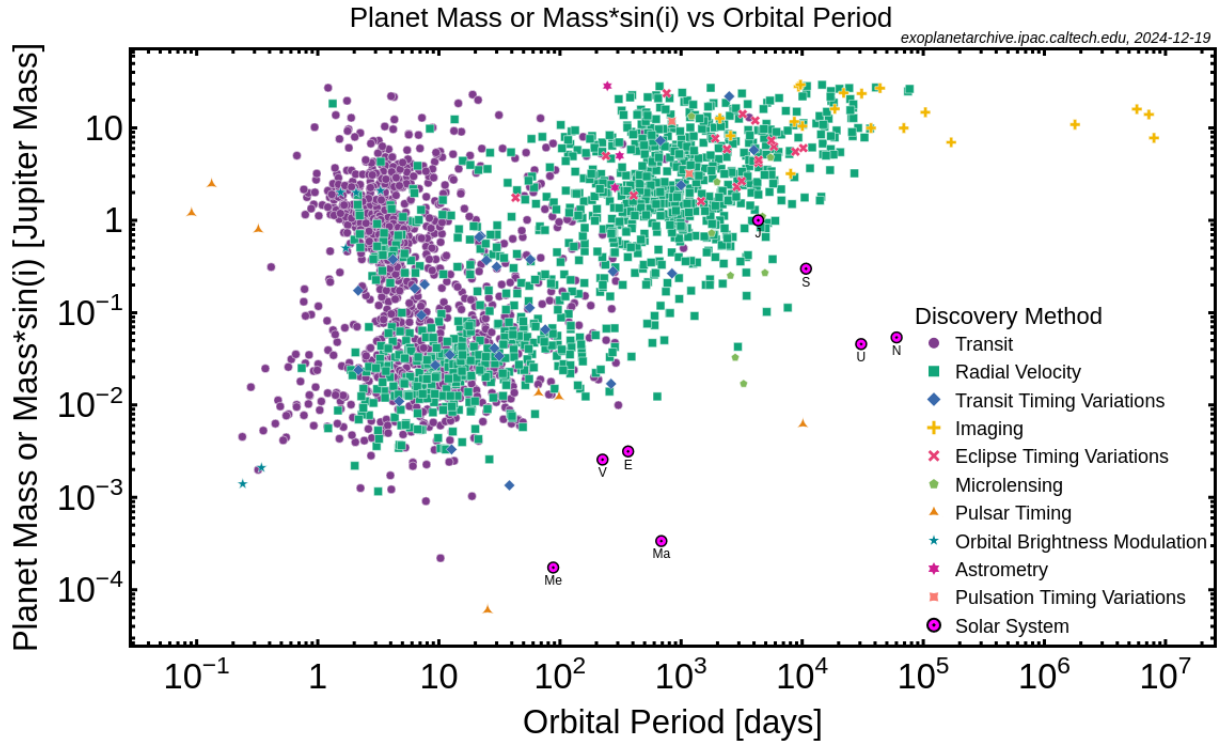


Figure 1.5: Mass- Period distribution for various exoplanet distribution techniques. Image courtesy: [NASA Exoplanet Archive](#)

1.2.1 Science objectives

The advancements in research topics dependent on the variability of stars and light curves have presented a strong case to obtain more and better photometric data through upcoming space missions like PLATO. As discussed above the core goal of PLATO is to look for earth-sun analogs based on which the overall mission is designed. The mission is designed to focus on comparatively bright targets with Visual magnitude (V) less than or equal to 11 so that a ground-based high-precision radial velocity follow-up is possible to estimate parameters like the planet's mass and radius with high accuracy.

But, PLATO won't be limited to just one goal as photometric data of targets from different ranges of both stellar and planetary masses with different periods will also be obtained which will be useful in probing into cases like exoplanets around massive stars. Apart from this PLATO will also provide the photometric data of stars in its field of view required to study other phenomena responsible for temporal variability in the observed flux of the star. Hence, the light curves extracted through PLATO data products will

Table 1.1: Brief overview of all stellar samples from asPIC.

Sample	Number of stars	Spectral type	Visual Magnitude
P1	15000	F5-K7	11
P2	1000	F5-K7	8.5
P4	5000	M Dwarfs	16
P5	245000	F5-late K	13
color sample	300	Anywhere in the HR diagram	-

be responsible for loads of research in fields like asteroseismology, eclipsing binary stars, extragalactic astrophysics, etc. Hence, a detailed overview of the core and complementary science goals of PLATO has been documented in the PLATO science requirements document¹ ([Rauer et al., 2024](#)) .

1.2.2 PLATO image and data acquisition

An important aspect of the PLATO mission is the extraction of the data corresponding to targets of interest within the FoV of the telescope. For this purpose, the all-sky PLATO input catalog (asPIC) ([Montalto, M. et al., 2021](#)) having 2,675,539 targets of F, G, K and M type dwarfs has been developed based on the astrometry and photometric data from Gaia DR2. To fulfill the major science objectives of PLATO, the entire catalog is divided into 5 samples namely P1, P2, P4, P5, and a color sample that will observe stars in red and blue bands at different wavelengths. The sample P3 has been eliminated for historical reasons ([Montalto, M. et al., 2021](#)). The description of all the samples is described in table1.1. Light from a particular star will be incident on a small subfield of CCD corresponding to its location. Hence, all the targets from asPIC are assigned to a 6×6 subfield of CCD called an imagette. This imagette is an essential data product through which the photometry of all the targets will be processed and/or reduced on-board. This acquisition technique reduces the volume of data transferred from the telescope.

1.2.3 payload

The PLATO payload consists of 26 cameras, out of which 24 are Normal Cameras (N-CAMs), focusing on objects with a visual magnitude V fainter than 8, with a cadence of 25 seconds. The remaining 2 cameras have a very high cadence of 2.5 seconds and are hence called Fast Cameras (F-CAMs), designed to focus on objects with a V magnitude between 4 and 8. The F-CAMs are equipped with red and blue filters providing us with color information. The N-CAMs are further divided into 4 groups of 6 cameras, as shown in Figure (1.6). All the cameras in a group have the FoV of 1037 deg^2 , but all the groups are tilted by 9.2 degrees in different directions with respect to the 619 deg^2 FoV of the F-CAMs, which is parallel to the z-axis of the payload module. The different tilt directions in the N-CAM groups create a wider effective FoV of PLATO, which is 2232 deg^2 , with overlap of target objects observed from different groups, as shown on the right side of Figure 1.6. There are different regions in PLATO's global field of view with a different number of cameras focused on them, yielding different Signal to Noise

¹[PLATO science requirements document](#)

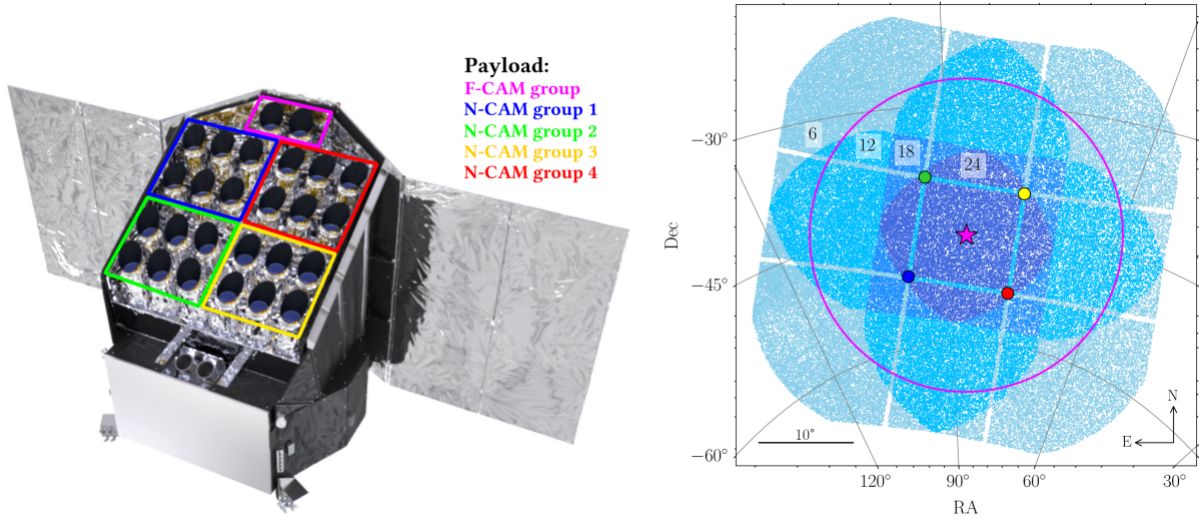


Figure 1.6: Left: PLATO multi-camera layout showing the locations of different N-CAM groups and the F-CAMs on the top. Right: Overlap in the field of view by different camera groups showing regions with Number of cameras(n_{cam}) = 6, 12, 18, 24 represented by different shades of Blue. image courtesy: ([Jannsen et al., 2024](#))

Ratio (SNR) ([Pertenais et al., 2021](#); [Jannsen et al., 2024](#)). Each camera setup comprises a Telescope Optical Unit (TOU), which is a fully dioptric telescope with 6 lenses each, a Focal Plane Assembly (FPA) having 4 CCDs with 4510×4510 pixels each, a Front end electronics (FEE), and a FEE support structure (FSS). Apart from the camera setup, the payload also consists of 13 onboard Data Processing Unit (DPU), each responsible for processing the data from the CCDs of 2 cameras into cadences of 25s for N-CAMs and 2.5s for F-CAMs before sending to Instrument Control Unit (ICU), which compresses the data and sends it to the ground for further correction and scientific analysis later on ([PLATO Defination study report, 2017](#)).

1.2.4 PLATO Noise contributors

The signal obtained by PLATO is a result of different photo-electrons sources captured by the CCD pixel and the effect of noise sources from the instrument. The desired stellar signal consisting of dominating photon noise combined with the background noise from the sky due to sources such as zodiacal lights, cosmic rays, and contamination from nearby stars contributes to the total number of released photo-electrons. There are a lot of instrument-induced effects that also contribute to the total noise budget of the telescope. Some of these major sources used by ([Börner et al., 2024](#)) in estimating the noise budget of PLATO and by ([Jannsen et al., 2024](#)) in the development of an end-to-end PLATO camera simulator are:

- **Charge Transfer:** CCDs being light-sensitive shift registers, can result in the transfer of charge from one pixel to another. The amount of charge transfer is dependent on the location of the pixel which is illuminated by the starlight with respect to the pixel that is receiving the transferred charge.

- **Dark Signal:** The thermal electrons emerging from the detectors also known as dark signal are also one of the contributors of noise. These electrons can also be generated in the absence of stellar photons.
- **CCD Smearing:** The cadence of 25 seconds in normal cameras consists of 21 seconds of exposure time where the target is observed followed by 4 seconds for the readout. But, during this readout time, the light incident on the telescope is not blocked by the telescope and leads to the smearing of photons in the CCD column where the signal is being transferred, also called as CCD smearing
- **Spacecraft Jitter:** The movement and instabilities of the spacecraft cause slight movement of stars on the CCD. This can degrade the quality of the image and can also lead to PSF blurring. Spacecraft jitter is the leading instrumental noise contributor at higher frequencies.
- **Noise from FEE:** There are 2 kinds of noise associated with FEE of the telescope namely FEE readout noise caused by the output amplifier and FEE offset noise caused by inaccuracies in temperature measurements of FEE.

Additionally, the overall motion of the telescope relative to the star's position causes a drift in the position of the star on the camera called the kinematic aberration. Kinematic aberration can result in the shift of star position by up to 0.5 pixels every three months. Similarly, such a shift in the star's position can also result from the 90-degree rotation of the telescope after every 3 months. This reorientation is necessary to maintain the telescope's solar panel in the direction of the sun. The drift occurring from this phenomenon can be up to 0.8 pixels every quarter making the total drift of 1.3 pixels ([Samadi R. et al., 2019](#)). This drift is constantly corrected by the Attitude and orbit control system(AOCS) of the telescope but the correction is not accurate due to the radially asymmetric nature of the drift. Hence, this effect proves to be a challenge in detecting signals in the obtained light curves and must be considered while estimating the total PLATO noise budget ([Jannsen et al., 2024](#)). The total noise budget of PLATO takes all of these noise sources into account. The domination of total noise represented by the Noise-to-Signal Ratio (NSR) varies with V as shown in Figure 1.7. As the magnitude of the star increases the noise starts to dominate over the signal received from the target star.

1.3 Focus of this study

In the above section, we discussed the effects that various types of noise sources can have on the data received from PLATO. Such effects can be significant in hindering both core and complementary science goals of the mission. Hence, thorough testing of telescope performance and efficiency in the presence of all the possible limitations must be done separately for all the science goals. For it's core science goal of detecting earth-like exoplanets around Solar-type stars, PLATO's predictive performance considering all the limiting factors has already been tested by ([Jannsen et al., 2024](#)). Testing for other complementary science goals such as eclipsing binary and exo-moons have been covered in previous master theses at KU Leuven. But, PLATO's potential to detect transiting exoplanets for high mass stars where the transit depth and consequently SNR drops due to its dependency on the stellar radii as shown in equation 1.3 remains unexplored.

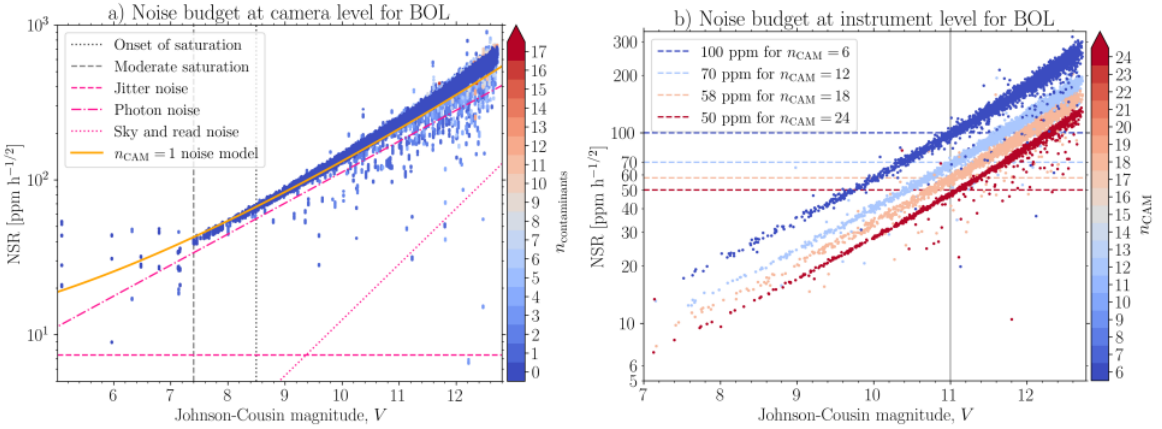


Figure 1.7: a. Noise budget of PLATO at camera level with the effects of Photon, Jitter, and Background noise. b. Noise budget for n -cams $\epsilon \{6,12,18,24\}$ at the instrumental level. Image courtesy: ([Jannsen et al., 2024](#))

The entire transiting exoplanet research has not yet been quite successful in discovering exoplanets for higher mass stars especially of spectral type A and above due to the lack of required high precision in current space telescopes. Hence, the exploration of such cases is vastly dependent on PLATO. Hence, this research, in particular, focuses on the exoplanet detection efficiency of PLATO around stars that are more massive than the Sun. Additionally, as demonstrated through Figure 1.7 the increasing visual magnitude of the star is also responsible for the reduction of the signal strength and thus, the capabilities of PLATO for our science goals must be tested for stars with different visual magnitudes. For this purpose, Synthetic yet realistic data for various types of exoplanets at different orbital distances around intermediate-mass stars($1.2M_{\odot}$ to $2.6M_{\odot}$) with different brightness levels has been simulated accounting for all the instrumental, background and stellar noise. This thesis takes LOP of PLATO into consideration to obtain approximately 2-year-long synthetic light curve data for a large parameter space in the range suitable to address the science question.

Chapter 2

Data: Simulation, processing and Analysis

In this chapter, the entire process of simulating, reducing and analyzing the data is discussed in detail. As summarized previously, The detection of transiting exoplanets becomes more and more challenging with increasing stellar radius and decreasing SNR. To test PLATO’s transit detection capabilities in such low SNR cases, it is useful to consider a distribution of stellar, planetary and orbital parameters in a systematic and unbiased manner. But, firstly the software responsible for the simulation of data PlatoSim ([Jannsen et al., 2024](#)) along with some of its features used in the research has been introduced in section 2.1. In the next section an overview of the parameter space that serves as an input for the PlatoSim is discussed. The output from the simulator has been detrended and reduced before the transit retrieval and further analysis of the data is done with the use of Transit Least Squares (TLS) ([Hippke, Heller, 2019](#)).

2.1 PlatoSim

The noise sources of PLATO as discussed in chapter 1 may result in various challenges that can be critical to the performance and success of the mission. Identifying the effects that can limit the mission performance before the actual in-flight operations has become a common procedure for space-based missions. The development of mission-specific end-to-end data simulators has provided a robust way for scrutinizing the mission performance and confirming the scope of the expected goals of the mission. The PLATO Simulator or PlatoSim software is an end-to-end simulator that produces the expected CCD data from PLATO. The PlatoSim software is designed to consider and model for all the natural noise sources affecting the quality of obtained data that were discussed in the previous chapter. The software can generate synthetic light curve data for a small CCD subfield called imagette such that the simulation is focused on a target object and not the entire FoV. This feature of PlatoSim helps avoid computational and storage expenses, particularly in cases like this research where a large parameter space is simulated. The imagette of size of 6×6 pixels is a key data product of PLATO providing the photometry of all the targets. However, PlatoSim can customize the imagette size for more versatile simulations. The software utilizes the asPIC to get realistic targets for simulations and also replicates the surrounding field of view to account for the pollution of signal from

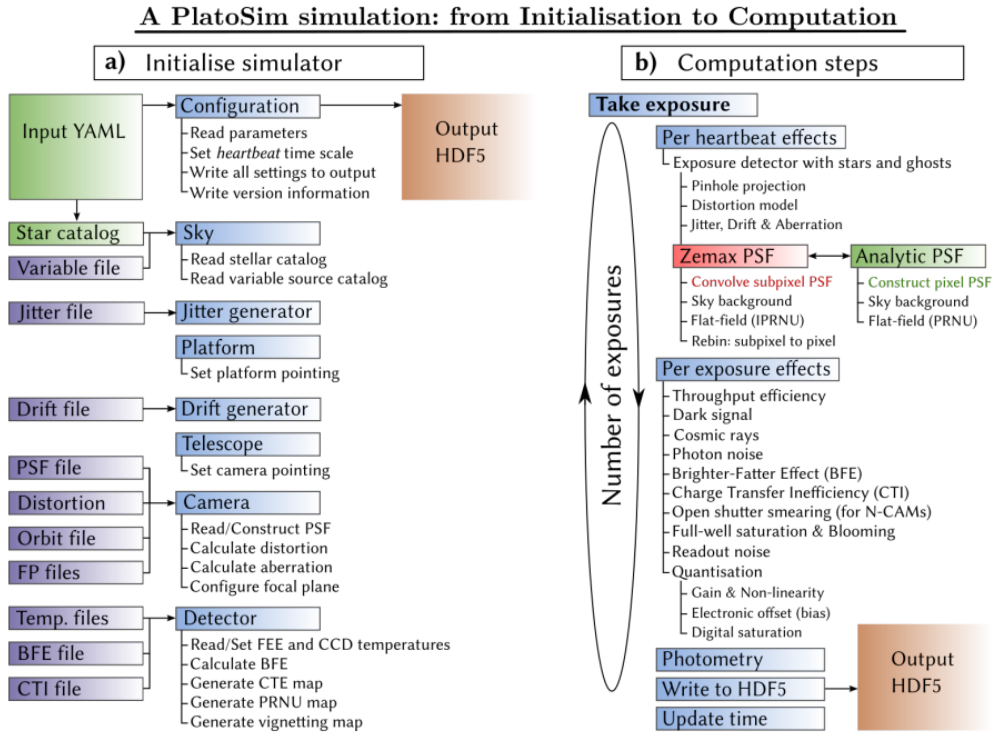


Figure 2.1: Tree diagram visualizing the architecture of PlatoSim software. Image courtesy: ([Jannsen et al., 2024](#))

the neighboring bright stars. This contamination has been quantified as Signal Pollution Ratio (SPR) by PlatoSim. The entire architecture of the software is illustrated in Figure 2.1. An input YAML configuration file that reads and initializes all the input parameters and a star catalog are the primary requirements to generate realistic time series data. It optionally takes a noiseless light curve as an input variable file along with different modules dealing with different noise effects originating from the camera, detector and sky background. Drift and jitter time series generators are implemented to introduce the effect of the pointing systematics. Then, PlatoSim step-by-step models and induces all the effects individually for several exposures as requested by the user. Once all of these effects have been induced to the input file, the photometric data of the target imagette per quarter is obtained separately for each camera CCD as an output.

Other than the generation of realistic light curves, PlatoSim is equipped with various features that are beneficial for this project. The most important feature of the software is the PLATOnium module which can simulate the light curve from multiple cameras for multiple quarters simultaneously. It provides realistic light curves by considering contaminants from the actual PLATO targets from asPIC. Another tool *varsim* is a module in PlatoSim that helps us in generating noiseless light curves required as an input for the output light curve generation. It takes various parameters as input and can generate light curves for the duration specified by the user. There is also the option of switching on/off the contamination effects from stars such as granulation and stellar spots. Additionally, the *utilities* module in PlatoSim has many helpful tools that help us in processing the data and is extensively used by PLATOnium and *varsim*. The tool has

many functionalities that can be useful in required data reduction procedures discussed in the later sections. The noise budget of PLATO for a given stellar magnitude can also be deduced from this module ([Jannsen et al., 2024](#)).

2.2 Parameter Space

The toolkit varsim takes various stellar, planetary and orbital parameters to model a light curve with an injected planet. All these essential parameters are classified into 1. primary parameters which will be defined by us as per the requirements of the project for example, the stellar mass distribution, types of planets injected and orbital distance, 2. secondary parameters such as stellar radius, effective temperature, orbital period, etc. that will correspond to the primary parameters and 3. independent parameters that are not very critical to the research outcome but essential for varsim to model the light curves.

2.2.1 Stellar Parameters

The hottest star around which an exoplanet transit has been detected belongs to the spectral type of A0/B9 with a stellar mass of $2.3 M_{\odot}$ ([Gaudi et al., 2017](#)). Massive main sequence stars of spectral type O and B have high stellar radii and luminosity making it extremely difficult to detect exoplanet transits. Hence, this research primarily focuses on stars from F9 type ($M_{\star} = 1.2M_{\odot}$) to A0/B9 types ($M_{\star} = 2.6M_{\odot}$). Precisely, 8 different bins of stellar masses between 1.2 to 2.6 were selected. Other secondary stellar parameters like stellar radii, metallicity, and temperature values corresponding to the selected stellar masses were deduced from the grid of Modules for Experiments in Stellar Astrophysics (MESA) models ([Paxton et al., 2010](#)). MESA is an open-source software used to computationally simulate and model stellar evolution for a wide range of astrophysical cases. All the deduced parameters correspond to the same stellar age of 3×10^8 years. This age has been chosen considering the shorter life span for higher mass stars and to have all our simulations within the main sequence phase of the star to maintain uniformity in our analysis. Figure 2.2 shows the variation of stellar radii and temperature with respect to the stellar mass obtained through the MESA models. The temperature of the stars increases with the mass of the star as more massive stars have stronger gravitational fields resulting in stronger core compression and faster nuclear fusion.

PLATO's noise budget as a function of visual magnitude as shown in Figure 1.7 indicates the increase of noise with the magnitude of the star. Therefore, the visual magnitude of the target star is a crucial factor affecting the NSR of the observed data. Thus, to include the contribution of stellar magnitude in our analysis, 5 different bins are selected from PLATO passband magnitude 8.5 to 16.5. The minimum value of the bin corresponds to the onset of saturation below which the mask size would exceed the dimension of imagette making it unsuitable for photometry as shown in Figure 1.7a. The NSR corresponding to the higher magnitude bins was calculated using the utilities module of PlatoSim as represented in Figure 2.3 which is the extrapolation of Figure 1.7. The NSR for photon, background, and jitter noise are calculated individually by the Utilities module. The aggregate NSR value can then be written as shown in the equation 2.1 given

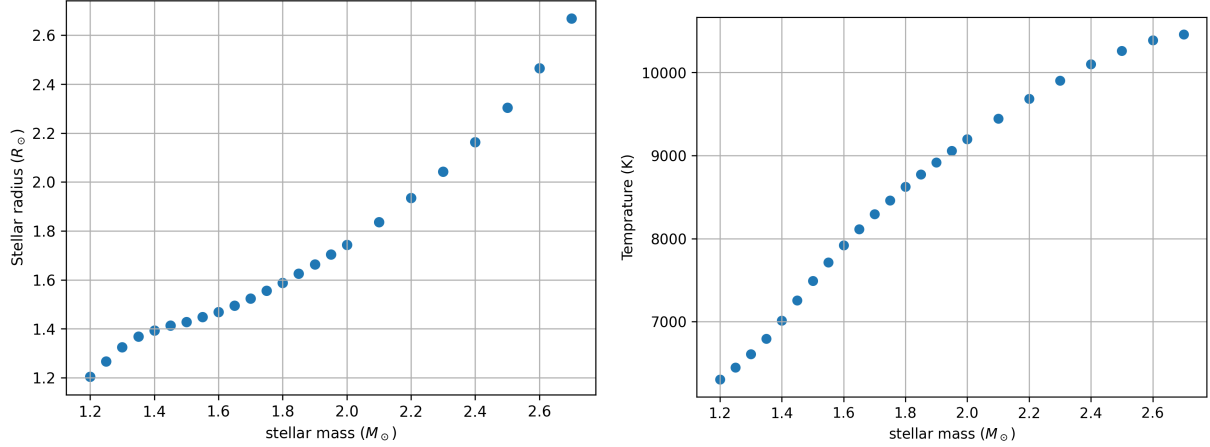


Figure 2.2: Left: Stellar radius as a function of stellar mass Right: Variation of effective temperature with stellar mass

by (Börner et al., 2024)

$$NSR_{tot} = \sqrt{NSR_{\text{photon}}^2 + NSR_{\text{background}}^2 + NSR_{\text{jitter}}^2} \quad (2.1)$$

Figure 2.3 shows a steep increase in the contribution of background noise around magnitude 15 and at 16.5 magnitude it overpowers the photon noise. Thus, this proves to be a good reason to have 16.5 as the upper boundary for our simulations.

2.2.2 Planetary parameters

As shown in Figure 1.5, There are planets with a wide range of masses and radii discovered through the transit method. Therefore, considering a range of planetary radii which can significantly alter the SNR of the transit is very essential for the completeness of the study. There are 6 different types of exoplanets chosen in this study out of which 3 have their physical parameters such as mass and radius primarily based on planets from our solar system. Based on these parameters, These 3 types will be referred to as "Earth-like", "Jupiter-like" and "Saturn-like" in the rest of the study. 2 exoplanets have parameters based on lower and upper bounds of a commonly discovered exoplanet type called super-earths having masses ranging from $2 M_{\text{earth}}$ to $10 M_{\text{earth}}$. There is also an extreme case selected with a mass typical of a brown dwarf but this mass can correspond to a planet that is accreting mass from its host star (Zhou et al., 2014). Planetary mass and radius values of this extreme case are based on an object that is at the brown dwarf/planet boundary detected and measured by (Zhou et al., 2014). The exact values of planetary mass and radius can be referred from table 2.1. The selection of exoplanets with different planetary radii ensures different SNR values per stellar mass bin.

2.2.3 Orbital Parameters

The duration and probability of transit also depend on the orbital position of the planet with respect to the host star as shown in equation 1.1. Hence, there are 5 different bins of orbital position covered for each configuration of stellar mass and planet type. The

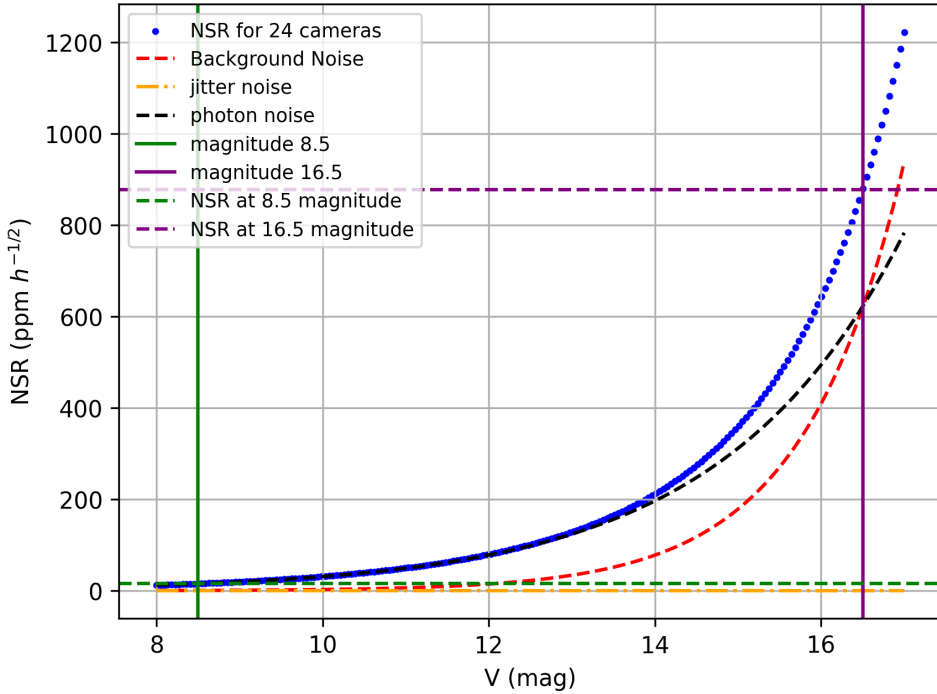


Figure 2.3: Noise budget of PLATO extrapolated upto the magnitude 17 using the PlatoSim. Noise budget for magnitude 8.5 and 16.5 has been highlighted using the green and purple dashed lines respectively.

Table 2.1: Planetary mass and radius of all the planets injected in the simulations.

Planet type	Planet Mass (M_{earth})	Planet radius (R_{earth})
Earth-like	1	1
Super earth 1	2	1.2
super earth 2	10	2
Neptune-like	17	3.9
Jupiter-like	318	11
Brown dwarf/planet boundary object	9800	52

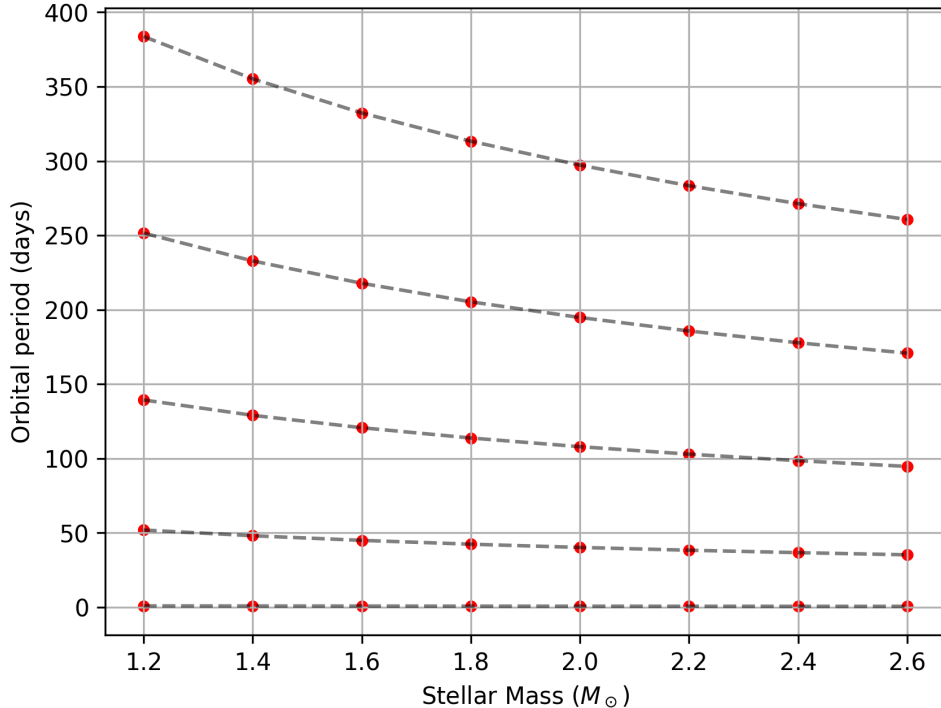


Figure 2.4: Variation of the orbital period with stellar mass for 5 fixed orbital distances.

orbital period, which is the direct input for Varsim is deduced for the star corresponding to the chosen orbital distances of stars from Kepler's 3rd law as shown in the equation 1.2. This equation showed the dependency of the orbital period on the stellar mass of the star. Hence, as we select 5 fixed orbital distances for each configuration, we will obtain different orbital periods for different stellar masses. This variation can be seen in Figure 2.4 where we see smaller orbital periods for higher-mass stars. This is observed due to higher gravitational influence from the higher mass stars.

Other orbital parameters can affect the shape of the transit but accounting for a distribution of all these parameters can be extremely expensive on the computation side. Therefore, all such parameters have been either picked randomly from a uniform distribution of suitable range or kept constant. The selection of such parameters is summarized in Table 2.2. The values of the orbital period for the entire period can be visualized from the Figure 2.5. We can see a fair distribution of values for eccentricity and argument of periapse in the respective desirable ranges.

Table 2.2: Selection of range for orbital parameters

Parameter	Distribution	Range Value
Inclination	constant	90 degrees
Eccentricity	uniform distribution	0 to 0.3
Argument of periapse	uniform distribution	0 to 180 degrees
Time of ephemeris	constant	15 days

The final parameter space covered in this research has 8 different stellar mass bins each consisting of 6 different exoplanets placed at 5 orbital distances from the host star. The

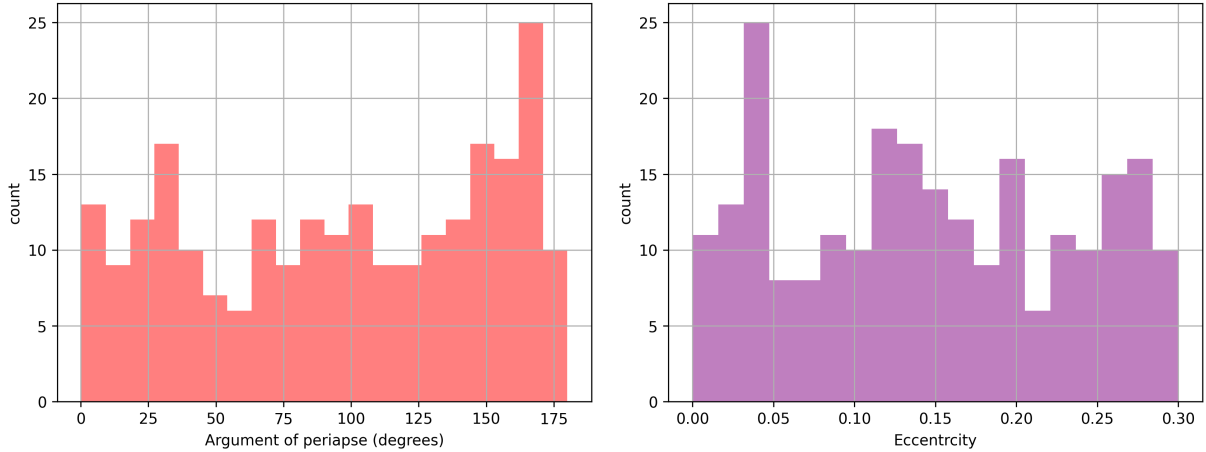


Figure 2.5: Histograms representing the distribution of orbital parameters for the parameter space. Left: argument of perihelion, right: eccentricity

simulation carried out for 5 different magnitude bins results in a total of 1200 different configurations. The entire parameter space with exact parameter values can be found in the appendix A.

2.3 Data Analysis

The light curve generated by PlatoSim can have variability in the signal corresponding to stellar and instrumental effects apart from the main transit signal from an exoplanet as discussed in chapter 1. These sources can hinder the detection efficiency and lead to inaccuracies in constraining the parameters of the planetary system. Hence, identifying these trends and removing them from the data, a process popularly known as detrending is an essential step in the procedure of transit retrieval. We make use of the Wōtan detrending package ([Hipke et al., 2019](#)), an open-source package that has a variety of detrending filters to remove instrumental and stellar variability from the data that can hinder the strength of the transit signal. The Turkey's biweight method ([Mosteller, Tukey, 1977](#)) from the Wōtan detrending package is used in our study. This package has been embedded in the PLATOnium enabling us to directly obtain a detrended light curve. Further, the data is binned into 10-min intervals to reduce the volume of data but at the same time, the transit signal is preserved. This process enables us to analyze the data more efficiently without losing valuable information. The final output of simulations received from PLATOnium contains time and relative flux for 720 days (8 quarters) along with metadata containing key statistics related to the quality of data and stellar contamination.

2.3.1 Transit retrieval

Once the data has been detrended and binned, it must be treated as realistic data obtained from PLATO. For the entire procedure of retrieving transits, it is essential to pretentiously forget the entire input planetary parameter space. This step ensures a realistic detection statistic without the presence of any bias. Hence, no part of the transit detection algorithm is fed with priors of planetary mass, radius, period, eccentricity, or inclination. The use

of input stellar mass and radius is permitted as it can be deduced from the GAIA catalog ([T. et al., 2016](#)) for the real PLATO targets. The TLS algorithm is used for the transit retrieval procedure. This algorithm is chosen over the traditional BLS algorithm ([Kovács, G. et al., 2002](#)) as it searches for transit-like features from the phase folded light curve. It considers ingress, egress and stellar limb darkening effects resulting in better detection efficiency, especially for smaller planets. An important statistical estimate for transit retrieval is the Signal Detection efficiency (SDE) which was first implemented in the BLS algorithm and optimized further in the TLS. SDE compares the significance of χ^2 minimum with the χ^2 landscape from the surrounding data. SDE can be written as:

$$SDE = \frac{1 - \langle SR \rangle}{\sigma(SR)} \quad (2.2)$$

where the SR- Signal Residue is calculated for binned data in BLS whereas the data is not binned in TLS resulting in higher sensitivity of The algorithm. This also makes TLS computationally more expensive. Figure 2.6 shows the analysis of Kepler K2-110b by [Hippke, Heller \(2019\)](#) using both the algorithms, clearly indicating a significant boost in SDE calculated by TLS over BLS. This boost results in an increase of true positives for lower SDE cases. This boost in SDE however doesn't boost the amount of false positives as shown in Figure 2.7. In this plot, 10,000 simulated light curves with an exoplanet and 10,000 simulated light curves without an exoplanet were analyzed through BLS and TLS. It can be seen that both cases result in 1 percent of false positives for the SDE threshold of 7. A more statistical comparison between BLS and TLS is shown in Figure 2.8 where 2346 planetary transit light curves from Kepler were analyzed using the BLS and TLS algorithms and a histogram of the reduced χ^2 residuals corresponding to both algorithms is plotted. As also shown by the equation above, the lower residuals from TLS guarantee a better SDE value and consequently more positive detection for lower signal strengths, which is typical in a lot of cases in this study.

The SDE has become a standard criterion in the exoplanet community to confirm the candidature of an exoplanet. [Hippke, Heller \(2019\)](#) further tested the TLS algorithm for the same 20000 simulated cases to determine the minimum Threshold of SDE for a transit detection to be counted as an exoplanet candidate also known as completeness of a transit. Any dataset with SDE below this threshold value which was estimated to be 9.1 has a more than 1/10000 probability of encountering false positives as seen in Figure 2.7. The same value of SDE has been adopted in our transit retrieval procedure. Additionally, another estimate that plays a key role in determining the completeness of exoplanet candidate and ruling out false positive detections is SNR. SNR of a planetary transit given by [Pont et al. \(2006\)](#) as shown in the equation 2.3.

$$SNR = \frac{\delta}{\sigma} \sqrt{N} \quad (2.3)$$

where, δ the transit depth is given by the equation 1.3, σ is the standard deviation of all the datapoints lying outside the transit and N is the number of datapoints inside the transit. The currently accepted minimum threshold for 100 percent completeness of a transit given by ([Pont et al., 2006](#)) is 7 and thus, same is adopted in this research.

After the TLS detects an exoplanet satisfying both the conditions as mentioned above, a model phase folded light curve is generated using it the BATMAN ([Kreidberg, 2015](#)) - an open-source Python software that can efficiently compute and model transit light

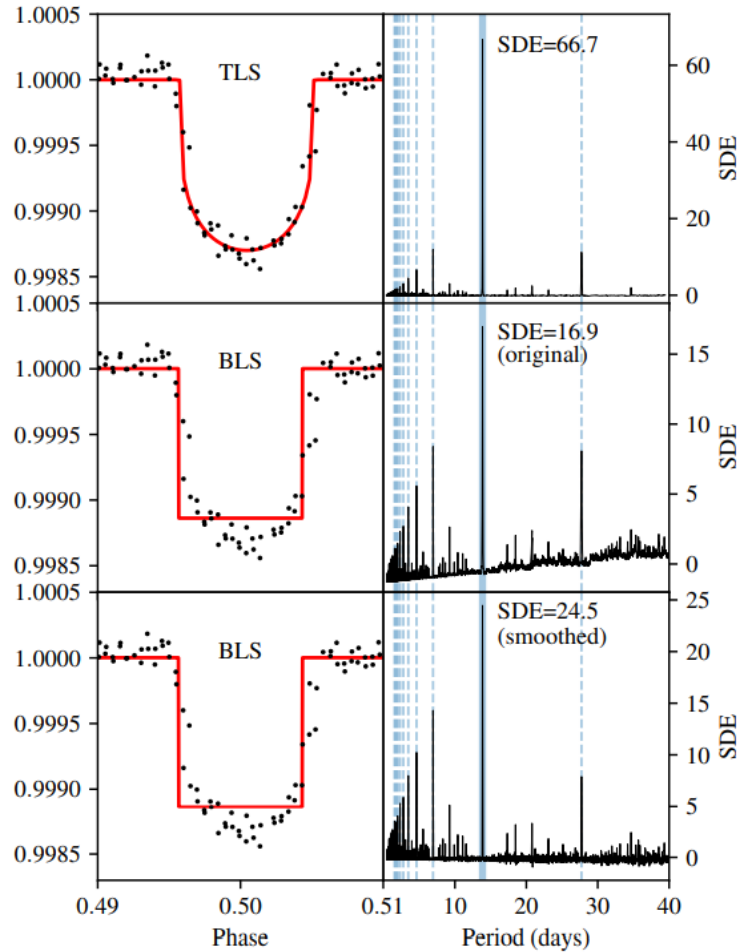


Figure 2.6: Comparison of transit retrieval and SDE of K2-110b using the TLS and BLS algorithms. Image courtesy: [Hippke, Heller \(2019\)](#)

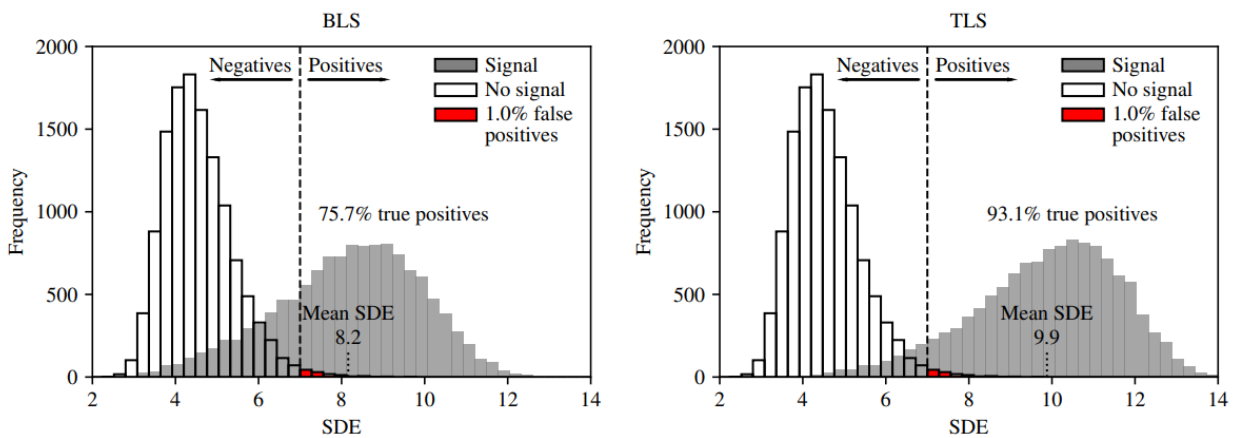


Figure 2.7: SDE statistics for 10,000 synthetic light curves with an injected exoplanet and 10000 synthetic light curves without exoplanet. Left panel: Transit retrieval through BLS algorithm, right panel: transit retrieval through TLS algorithm. Image courtesy: [Hippke, Heller \(2019\)](#)

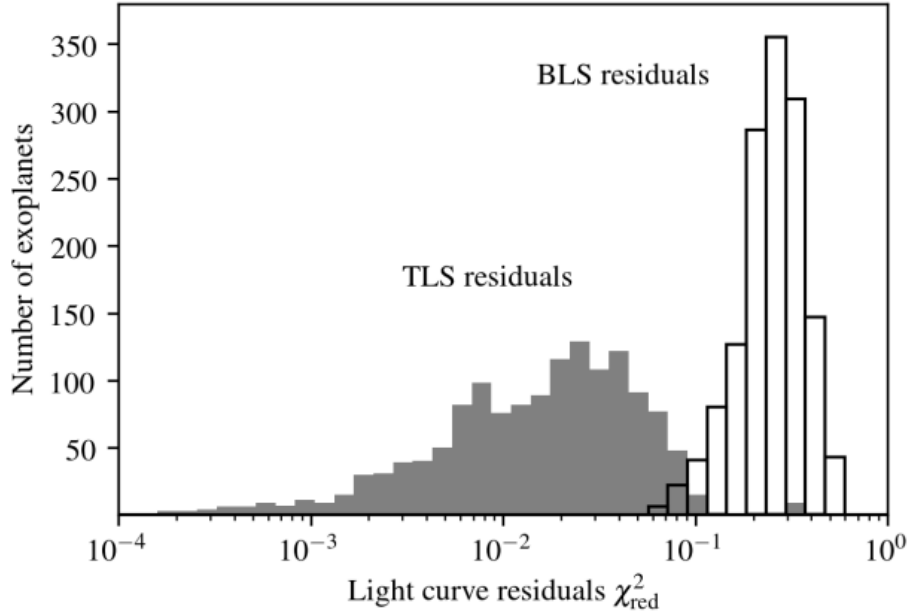


Figure 2.8: The reduced χ^2 residuals from BLS(open histogram) and TLS(gray histogram), calculated for 2346 planetary transit light curves from kepler. Image courtesy: [Hippke, Heller \(2019\)](#).

curves. The 3rd and final criterion to confirm the candidate is to manually verify the transit-like shape in the plotted phase folded light curve. Various types of outcomes are obtained once the transit retrieval algorithm is implemented considering all the three detection conditions discussed above. The first outcome is the true positive detection by TLS satisfying all three conditions. The second one is the outcome that suggests SDE or/and SNR values below their threshold values ring a strong false positive alarm. These detections are rejected and considered as no transit scenario. The third case arises from the quarterly gaps in the data resulting from the 90-degree re-orientation and signal transmission by PLATO. In this case, the SDE and SNR thresholds are achieved by the data gap which mimics an exoplanet transit. However, inspection of the phase folded light curve indicates a non-transit shape strongly suggesting further investigation.

An example of phase folded light curve that corresponds to a planetary transit is shown in Figure 2.9 whereas a false positive is indicated in Figure 2.10 where a clear data gap is detected as a transit by TLS algorithm. For such cases, the actual transit might still be present in the data but the SDE of period corresponding to the false signal is higher. Hence, for further analysis, we have plotted the SDE for all the periods as shown in Figure 2.11 and a phase folded light curve is manually modeled using the BATMAN software for the periods having the second highest SDE and so on until the desirable phase folded light curve is observed or the SDE and SNR have below threshold values resulting in the no-detection case. The SNR is recalculated for the new phase folded light curve using the equation 2.3. The phase folded light curve is plotted for the period corresponding to the correct SDE value. In some cases, it is required to further bin the data to observe the transit shape in the phase folded light curve as shown in Figure 2.12.

After all the steps, the final statistics for this research are obtained and will be discussed and visualized in the next chapter.

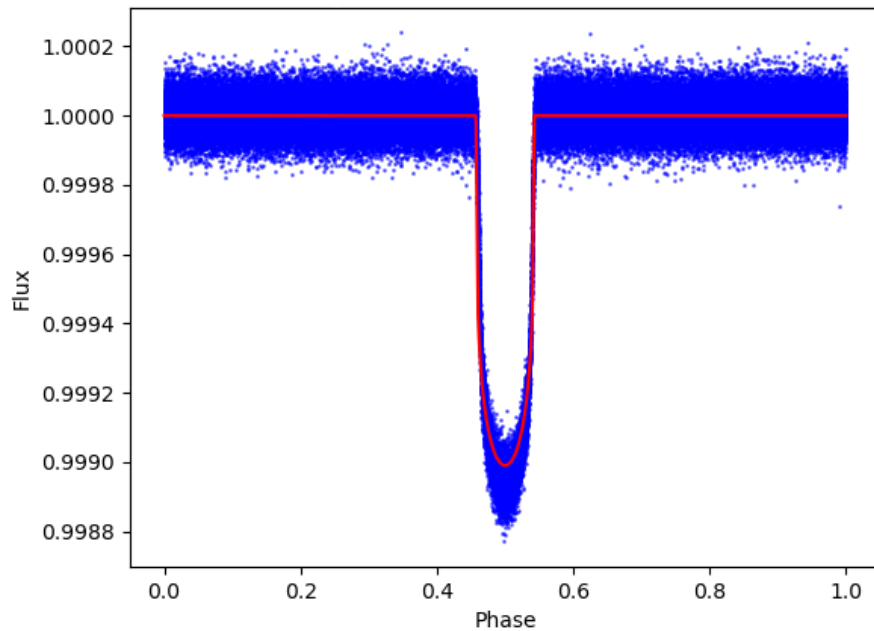


Figure 2.9: Phase folded light curve of planetary transit around a $1.2 M_{\odot}$ star simulated from PlatoSim and retrieved through TLS. The blue dots correspond to the simulated data and the red line shows the model of phase folded light curve generated with BATMAN

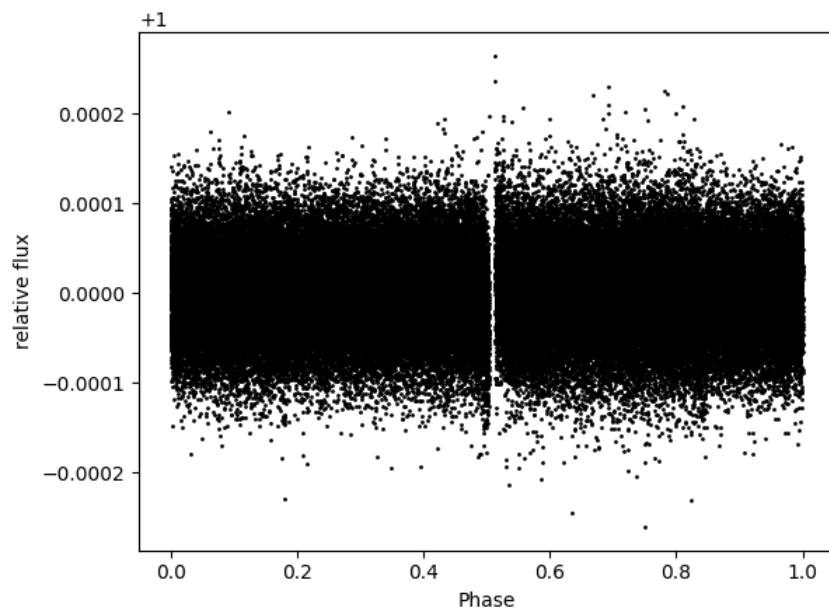


Figure 2.10: Phase folded light curve showing quarterly gap in the data

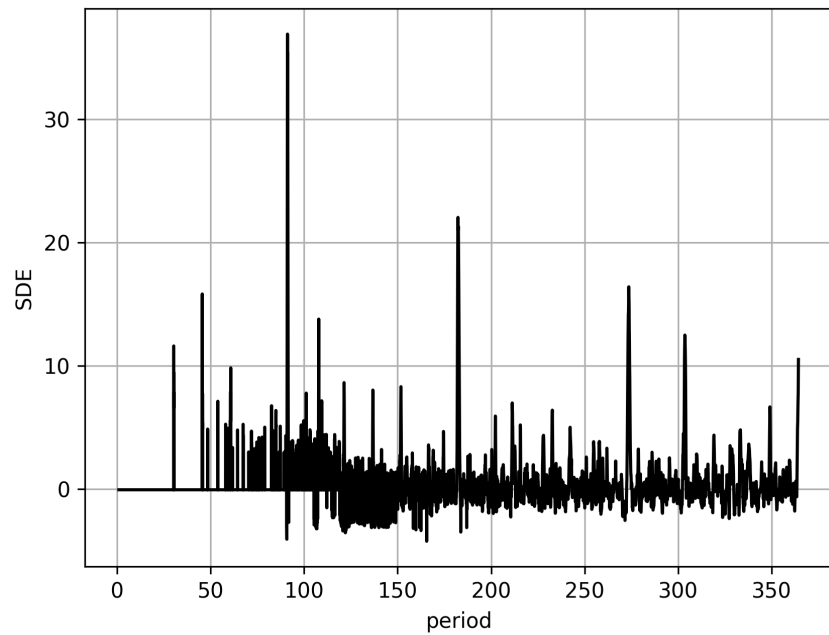


Figure 2.11: An example periodogram from TLS with highest peak corresponding to 90 days

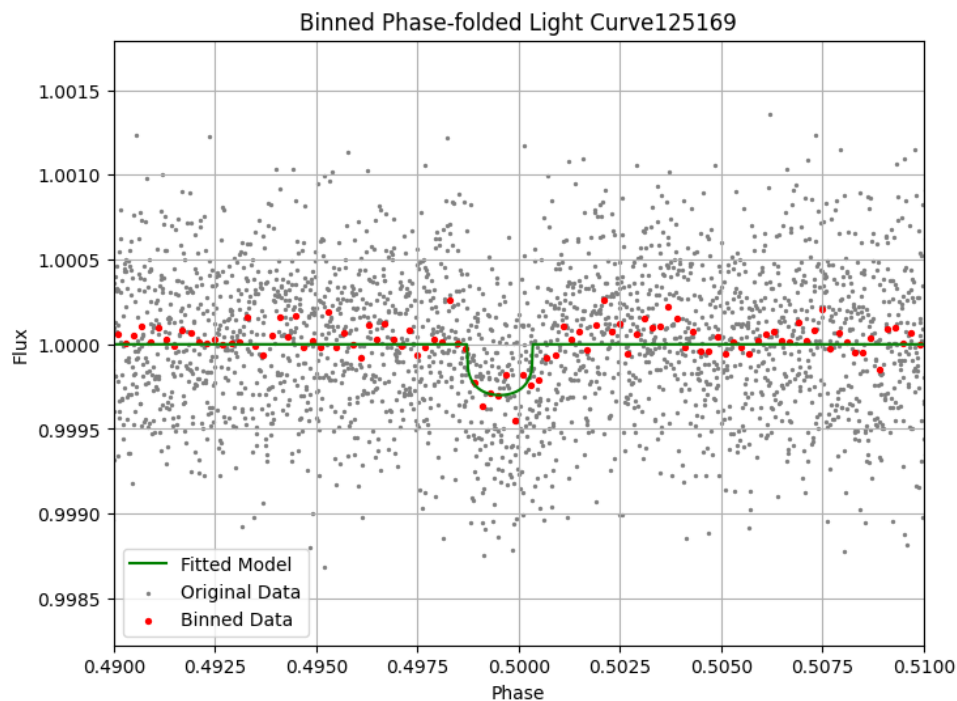


Figure 2.12: Simulated light curve from PlatoSim for a $2.2 M_{\odot}$ star of 12.5 magnitude (grey dots). Light curve of the same system in bins of approximately 1 hour (red dots). Model of the light curve created using BATMAN software ([Kreidberg, 2015](#)) (green curve).

Chapter 3

Results

In the previous chapter, we discussed the various steps undertaken in this research to simulate and test PLATO’s performance for exoplanets around A and F-type main sequence stars. After the data was simulated via PlatoSim for the appropriate parameter space, the post-processing of data was carried out making it ready for analysis through the TLS algorithm. In this chapter, we present the probabilities of detecting exoplanets as a function of stellar mass and PLATO magnitude. The accuracy in deducting the radii ratio from the observed transits is also explored and compared to the input value for the entire parameter space. Further, the significance of SPR on the detection statistics for all different magnitude bins is determined.

Before discussing the transit occurrence rates for our parameter space, we first visually examine and compare the introduction of noise in the input data for all the magnitudes. An example light curve of Jupiter-like planet around a $1.2 M_{\odot}$ star with the effects from all the possible sources induced by PlatoSim for all the magnitude bins is visualized in Figure 3.1. The noiseless input light curve has also been plotted for reference. The increase in the noise of the data with increasing visual magnitude agrees well with the predictions of Figure 2.3. As seen for the 16.5 magnitude plot, a planetary transit is not visible to the eye but such cases are still detected by TLS and visualized using processes like binning and phase folding the light curve as demonstrated in Figure 2.12. The re-orientation of the telescope after every quarter results in different noise levels for each quarter as seen in plots d,e, and f of figure 3.1 .

3.1 Transit occurrence rates

In chapter 2 we discussed the cases where the phase folded light curve suggested false positives due to quarterly gaps in the data. The detections from the TLS which doesn’t count for such cases can be seen in Figure 3.2. The cases that pass all the criteria and are detected directly by TLS are referred to as primary detections and the cases where the transit is retrieved after going through some extra manual steps are referred to as secondary detections in the rest of the research. The majority of detections that didn’t show an accurate planetary transit-shaped phase folded light curve even after binning had a light curve very similar to Figure 2.10 with period lying around multiple of 90-91 days which is a quarter. The histogram representing the period of such cases is represented in Figure 3.3 for all the magnitude bins. The cases in the plots corresponding to periods other than a quarter arise from other instrumental noise effects. The further scrutinizing of such

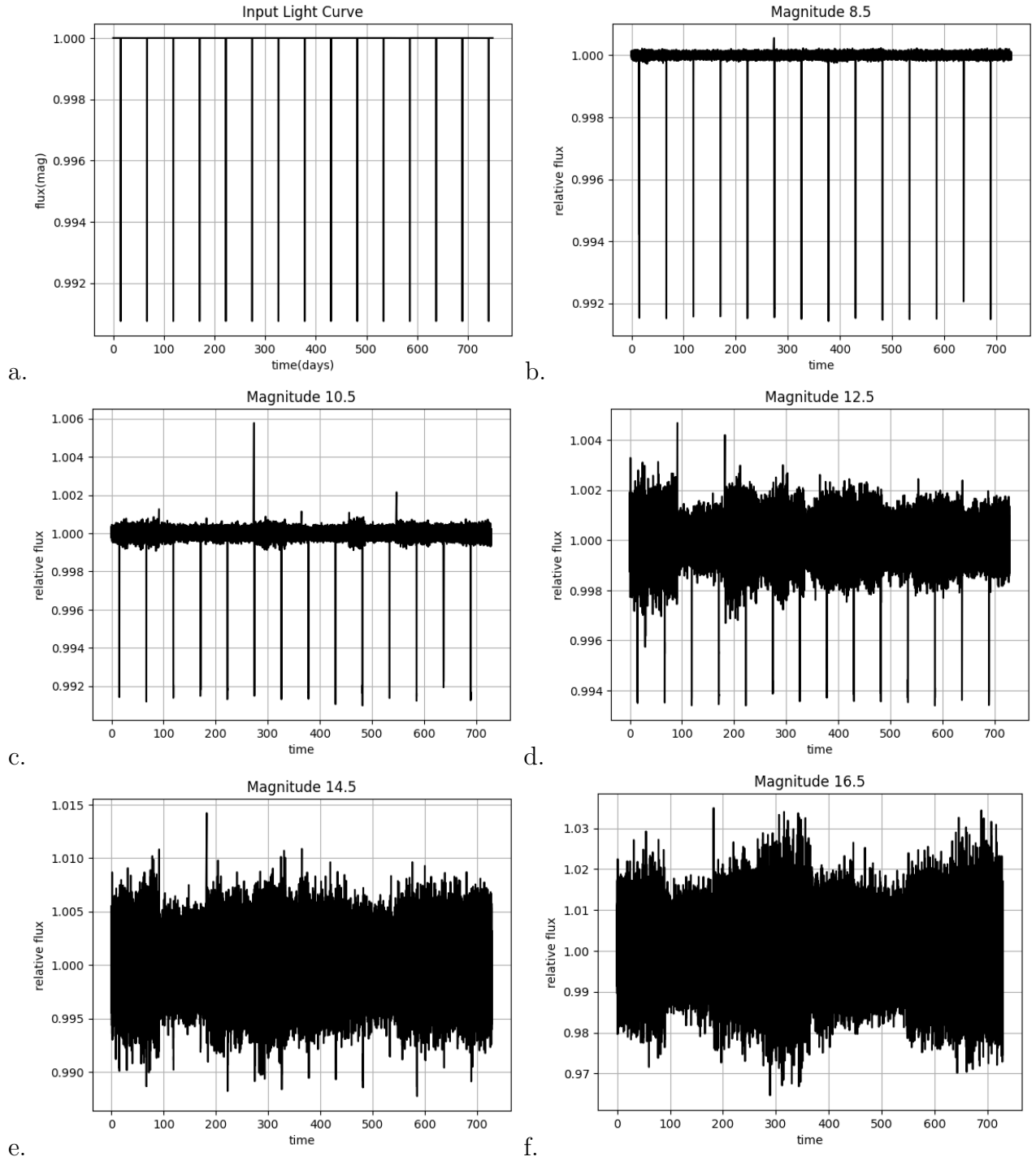


Figure 3.1: Light curves obtained through PlatoSim for Jupiter-like planet around a $1.2 M_{\odot}$ star. a. Input light curve from PlatoSim b. 8.5 magnitude system c. 10.5 magnitude system d. 12.5 magnitude system e. 14.5 magnitude system f. 16.5 magnitude system

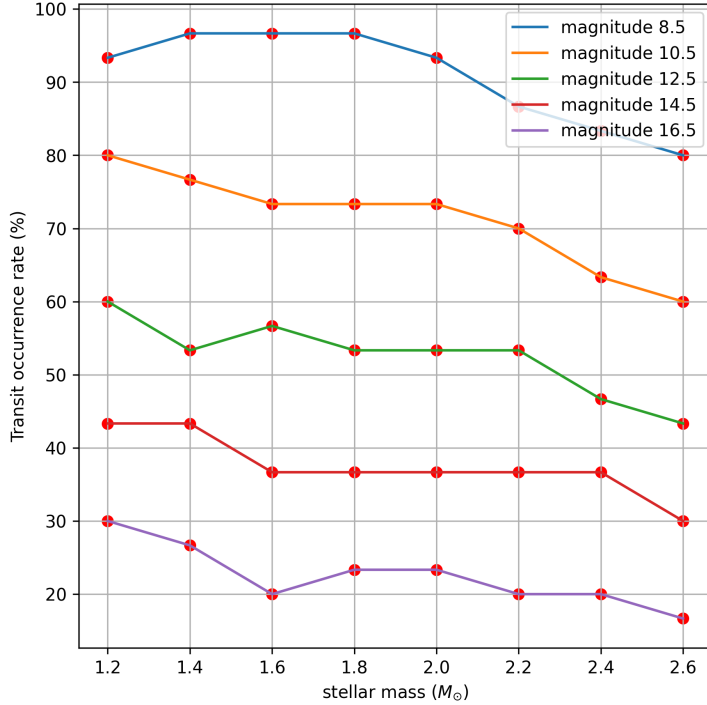


Figure 3.2: Transit occurrence rate from primary detections for each magnitude bin. This plot excludes the cases that required further analysis due to the presence of quarterly gaps in the data.

cases resulted in a better detection statistic compared to the primary detections and can be seen from Figure 3.4 for all the magnitude bins. Figure 3.4 shows a decline in detection fraction with the increasing stellar mass and also with increasing visual magnitude due to an increase in the contribution of noise sources. The detection of exoplanets around 1.2 to $2.0 M_{\odot}$ stars has a high transit occurrence rate as the SNR requirements are within reach of not only PLATO but other space telescopes from the past as well ([NASA Exoplanet Archive, 2024](#)).

The combined transit occurrence rate from all the magnitude bins corresponding to all the stellar mass bins is represented in Figure 3.5. A vital finding from this plot is a satisfactory Transit occurrence rate for the stars with higher stellar mass. The capability of PLATO in detecting more than 45 percent of planets for stellar masses above $2.3 M_{\odot}$ (highest stellar mass with a recorded planetary transit) opens up the doors for exploration of exoplanets in a range of stellar masses which has to date been unsuccessful in detection of exoplanets. Interestingly, if we focus more on the the brighter magnitudes, for example, magnitude 8.5 has transit occurrence rate of 84 and 80 percent for 2.4 and $2.6 M_{\odot}$ stars respectively. This result plays an essential role in determining the potential targets that can be significant in exploring the existence of exoplanets around intermediate-mass stars. However,a drawback of this visualization is that the overall detection rate in this Figure is majorly influenced by the significant lack of contribution from the higher magnitude bins. The percentage of planets retrieved by the systems corresponding to all the magnitude bins is represented in Figure 3.6. A 90.8 percent detection rate in 8.5 magnitude systems and a 22.5 percent rate in 16.5 magnitude systems indicates a major bias in the combined transit occurrence rates. Figure 3.7 shows a corre-

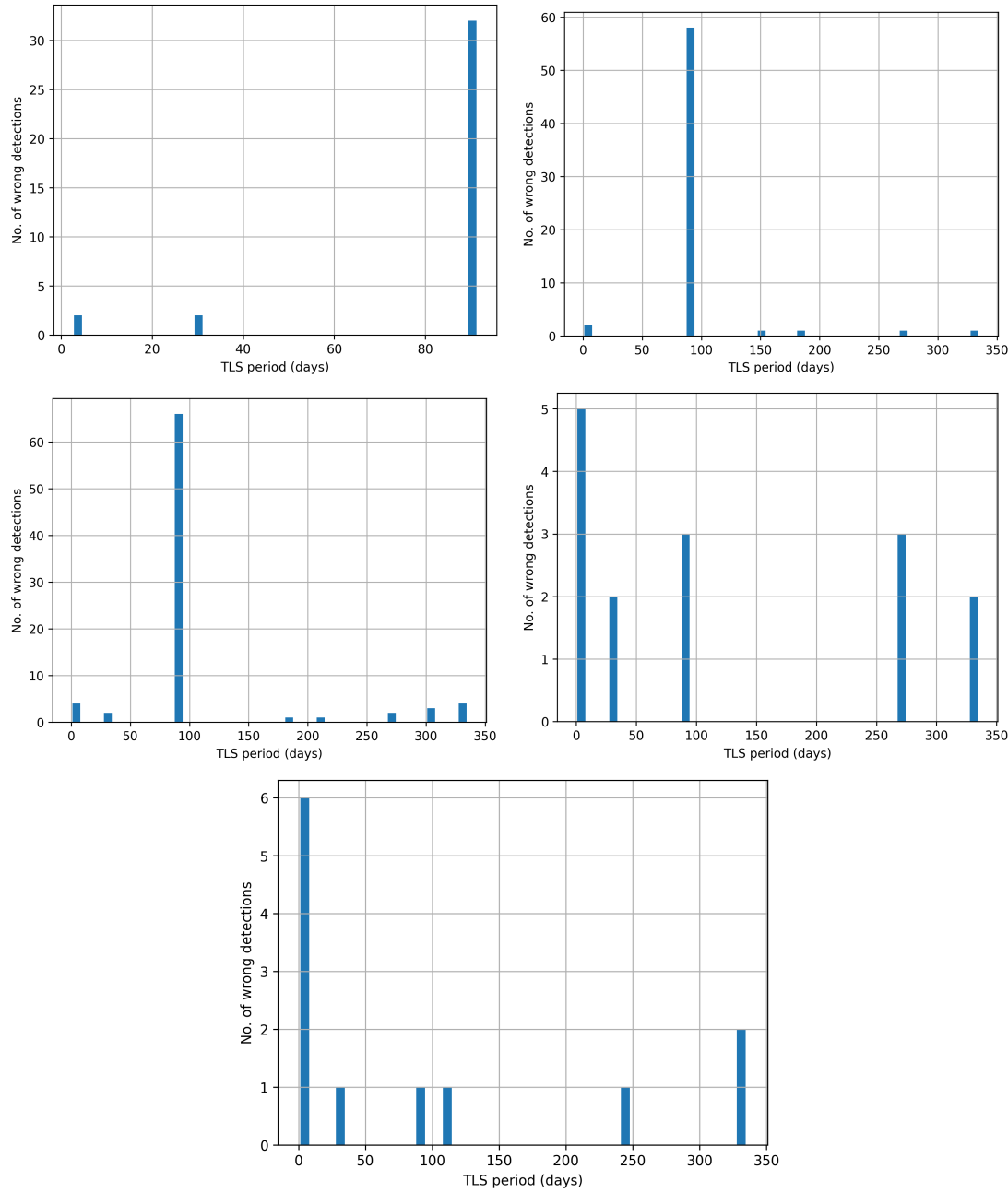


Figure 3.3: Histogram representing periods corresponding to false detections for: a. 8.5 magnitude b. 10.5 magnitude c. 12.5 magnitude d. 14.5 magnitude e. 16.5 magnitude

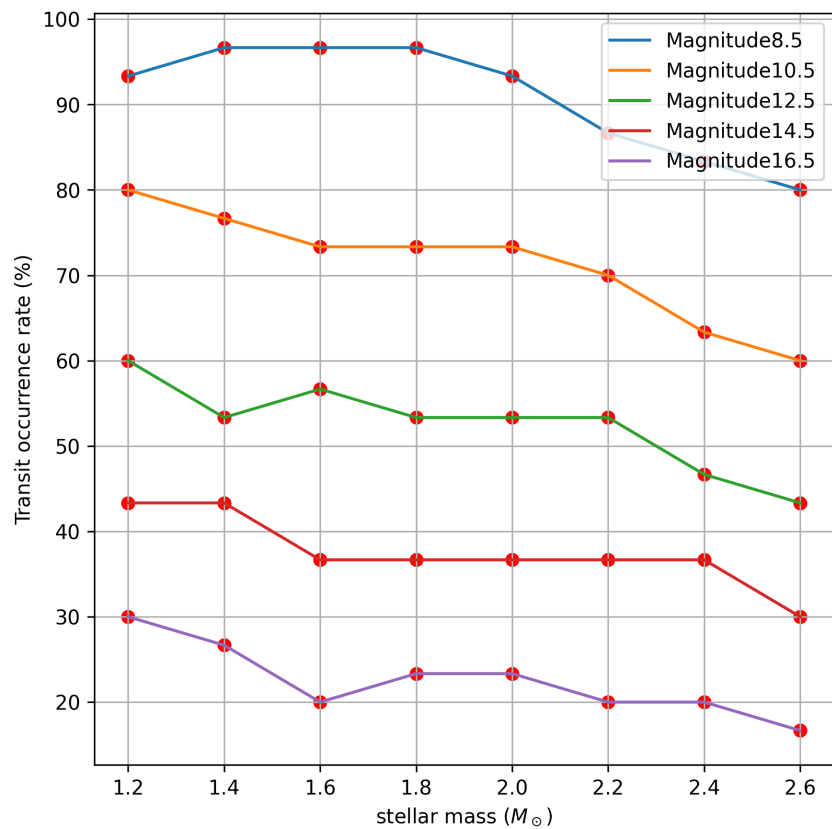


Figure 3.4: Transit occurrence rate from primary and secondary detections for each magnitude bin. This plot includes the cases that required further analysis due to the presence of quarterly gaps in the data

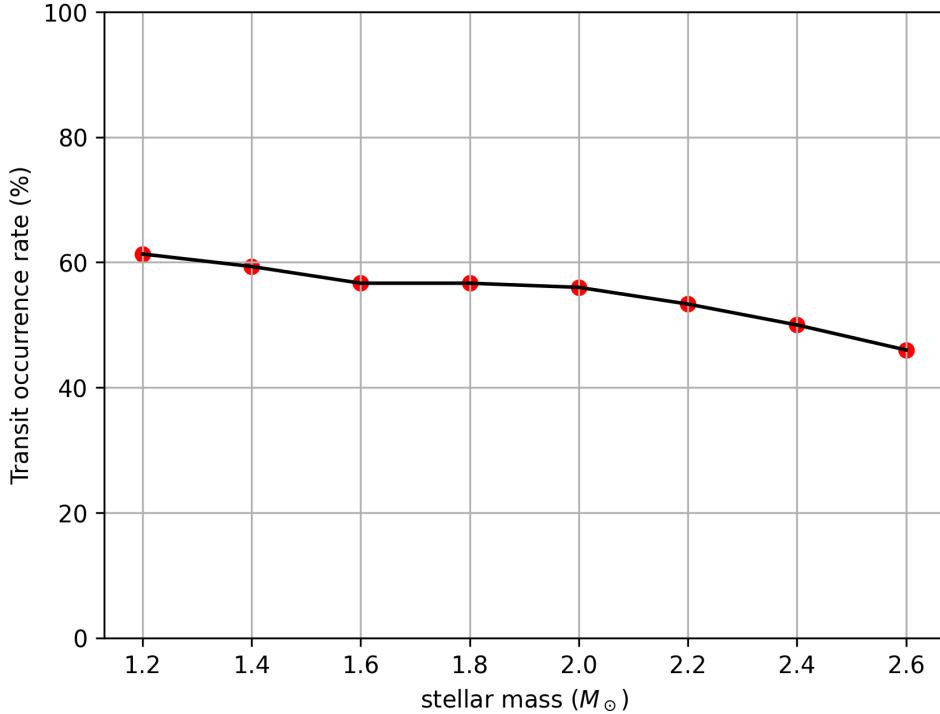


Figure 3.5: The total exoplanet Transit occurrence rate as a function of stellar mass.

lation matrix providing a better visualization for transit occurrence rates. The detection rate in each stellar and magnitude bin having 30 different input exoplanet systems can be observed in the plot making it easier to understand the parameter range with higher transit occurrence rates. The visualization gives us the exact idea of the limiting magnitude for PLATO’s exoplanet transit detection for each bin of stellar mass. There is a good probability for detection of exoplanets around $2.6 M_{\odot}$ stars if the visual magnitude of the stars is up to 10.5 magnitude.

As mentioned in chapter 2, 6 different types of exoplanets were injected in our data. A question that remains unanswered from the plots above is the transit occurrence rates corresponding to exoplanets of different sizes. Hence, the change in number of detections for different types of exoplanets in different magnitude bins is shown in Figure 3.8. Each type of exoplanet is simulated for 8 different stellar bins and 5 different periods per bin. Therefore, 40 configurations of each exoplanet type have been simulated per magnitude bin. Every pixel in the above plot represents the transit occurrence rate of a type of exoplanet in the corresponding stellar bin. From the plot, we can observe that in the 16.5 magnitude bin there are absolutely no detections for exoplanets that are smaller than Jupiter and a majority of the detections correspond to ‘brown dwarf/planet boundary’ objects. A significant reduction in the detection of earth mass planets can be already seen from magnitude 12.5. This observation aligns well with the threshold of $V < 11.5$ set by PLATO Mission Consortium (PMC) while preparing the catalog for its core science goal. Similar to the previous plot this illustration also indicates the limiting magnitude for detection of exoplanets of different sizes around stars with mass greater than $1.2 M_{\odot}$.

The combined dependence of the transit occurrence rate on both the stellar and planetary radii can be studied by plotting a similar correlation matrix for the expected transit

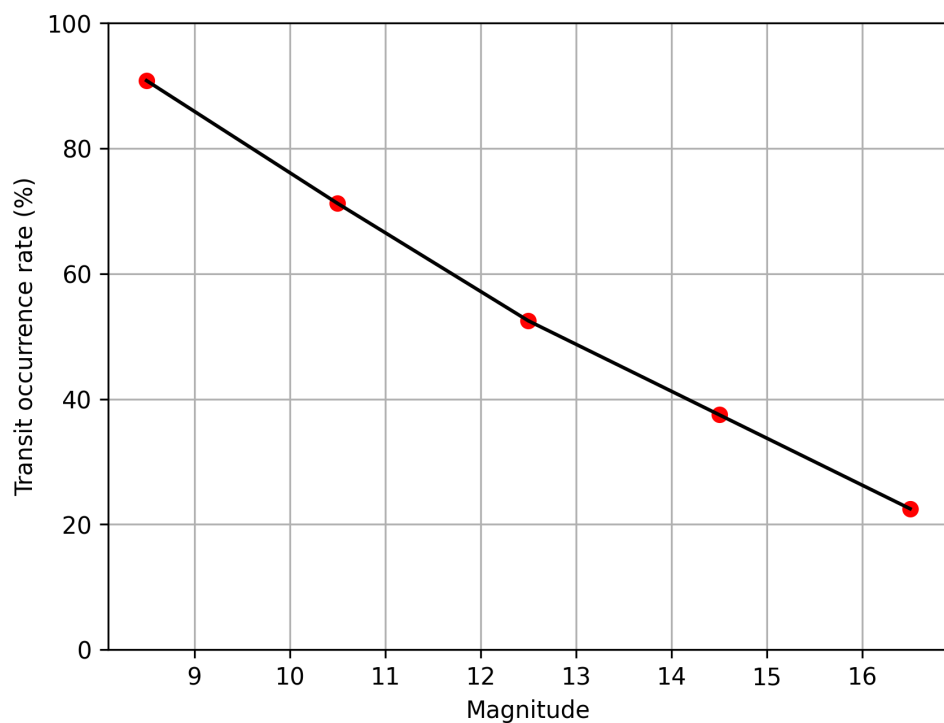


Figure 3.6: Transit occurrence rate for each magnitude bin.

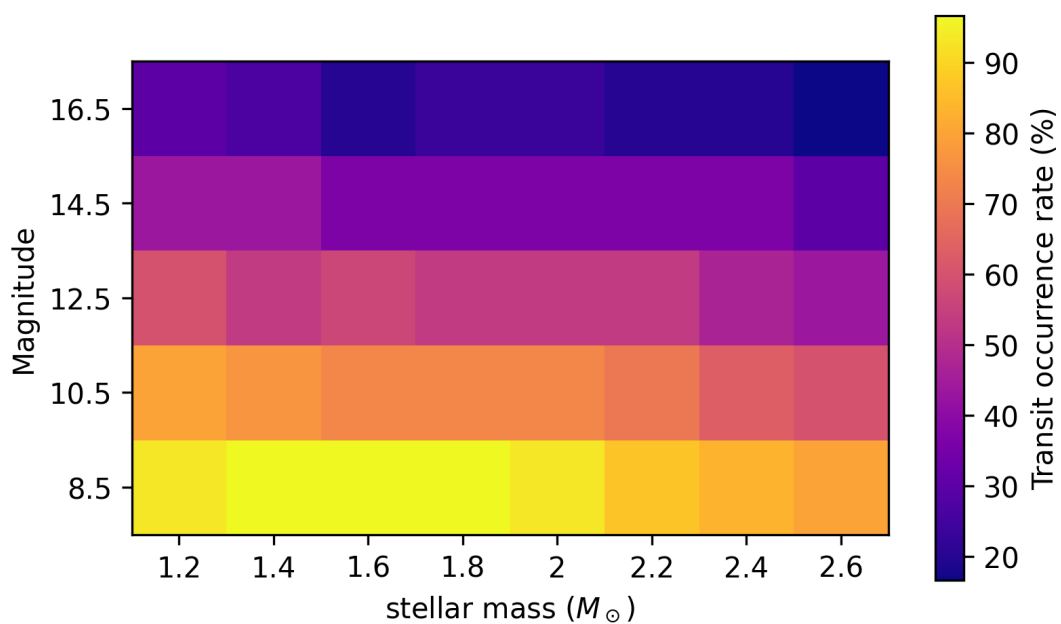


Figure 3.7: The correlation matrix representing the transit occurrence rate in each stellar mass and visual magnitude bin.

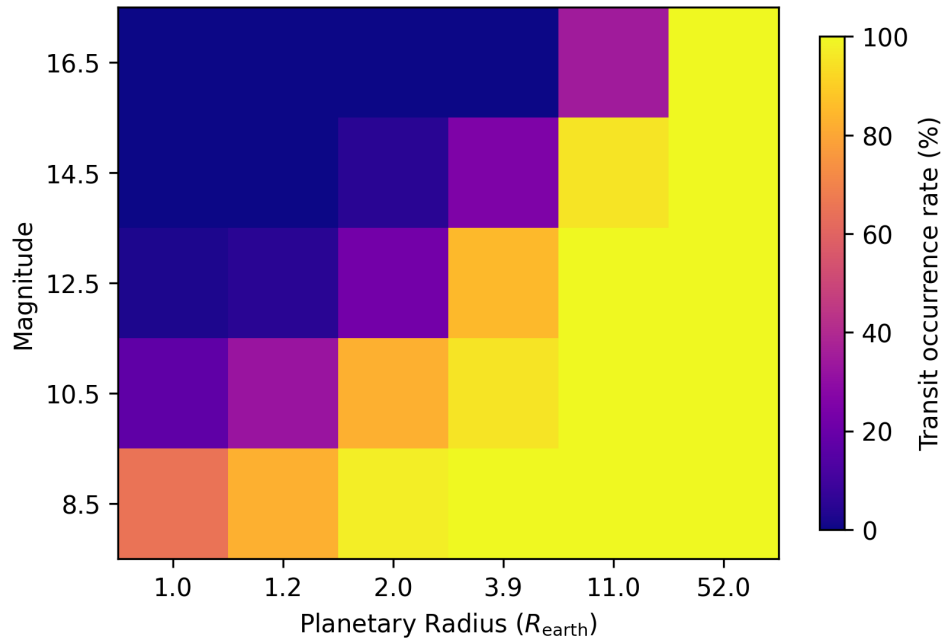


Figure 3.8: The correlation matrix representing the transit occurrence rate for each type of exoplanet in all the magnitude bins.

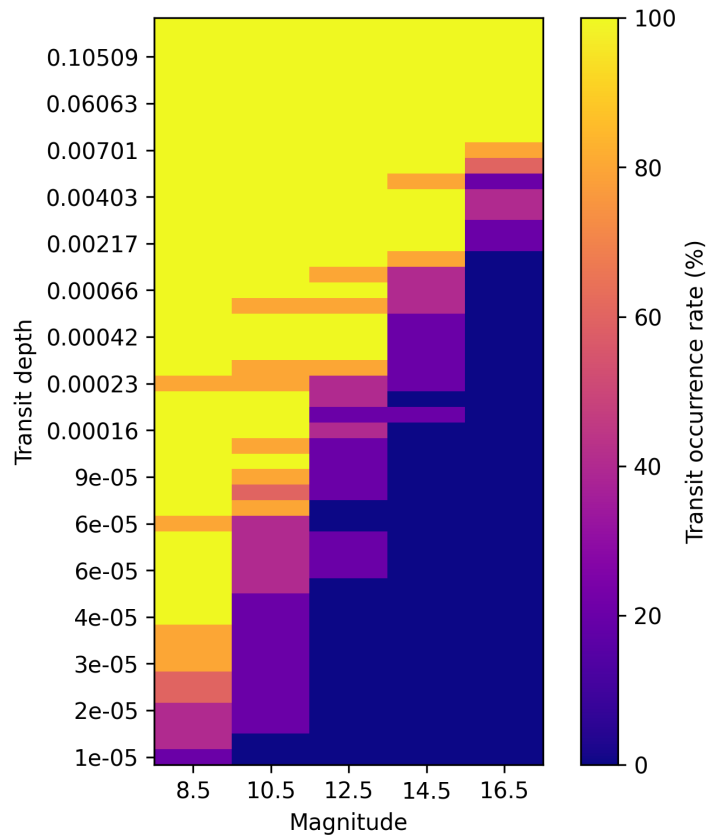


Figure 3.9: The correlation matrix representing the transit occurrence rate for all the transit depths in each visual magnitude bin.

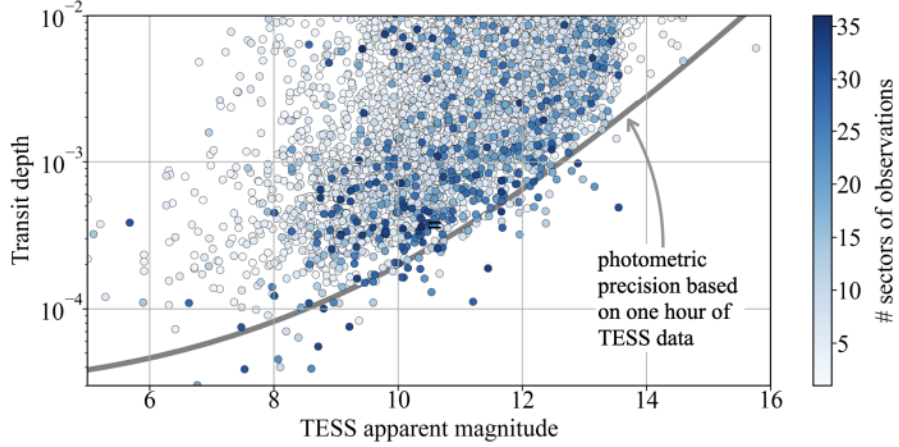


Figure 3.10: Transit depth of all TESS objects of interest excluding the known false positives plotted as a function of the apparent magnitude of the host star. Image courtesy: ([Winn, 2024](#))

depth from the simulations as illustrated in Figure 3.9. Figure 3.10 shows a similar analysis done by [Winn \(2024\)](#) for the TESS where the transit depth for all the TESS Objects of interest (TOIs) are plotted against the apparent magnitude. We can see a similar trend being followed in both cases where an increase in the magnitude reduces the transit occurrence rate for systems with smaller transit depth.

3.2 Radii ratios and uncertainties

Delivery of accurate planetary parameters from the PLATO mission plays a vital role in the study of characterization of different exoplanet systems. The ratio of planetary radius to the stellar radius i.e. $\sqrt{\delta}$ (see equation (1.3)) referred as radii ratio in this study is an important estimate to determine the accuracy and uncertainty associated with our transit retrieval procedure and the PLATO mission. The estimates of radii ratios for primary and secondary detections are obtained using the TLS algorithm and the BATMAN model respectively. These estimates are compared to theoretical values of the radii ratios determined from the equation (1.3). Figure 3.11 shows the estimated and theoretical radii ratio values for all the successfully retrieved transits in the analysis for all the magnitude bins. A clear linear correlation is seen between theoretical and estimated values for the majority of the cases as expected, with a few deviations that indicate the inaccuracies in the the estimated values.

This contribution of the 2 extreme magnitudes 8.5 and 16.5 can be seen separately in Figure 3.12. This figure reveals that the higher magnitudes especially 16.5 magnitude systems are majorly responsible for the inaccurate radii ratios seen in the previous figure. For brighter systems, a strong agreement between theoretical and estimated value of radii ratios is observed implying good precision in the retrieval of the ratio of radii. We can also see an underestimation of the radii ratios in majority of the cases due to noise sources resulting in more than expected photons being captured by the telescope during the transit duration. This results in dilution of the transit depth because of instrumental effects and contamination from other stars making it difficult to determine the true transit depth of

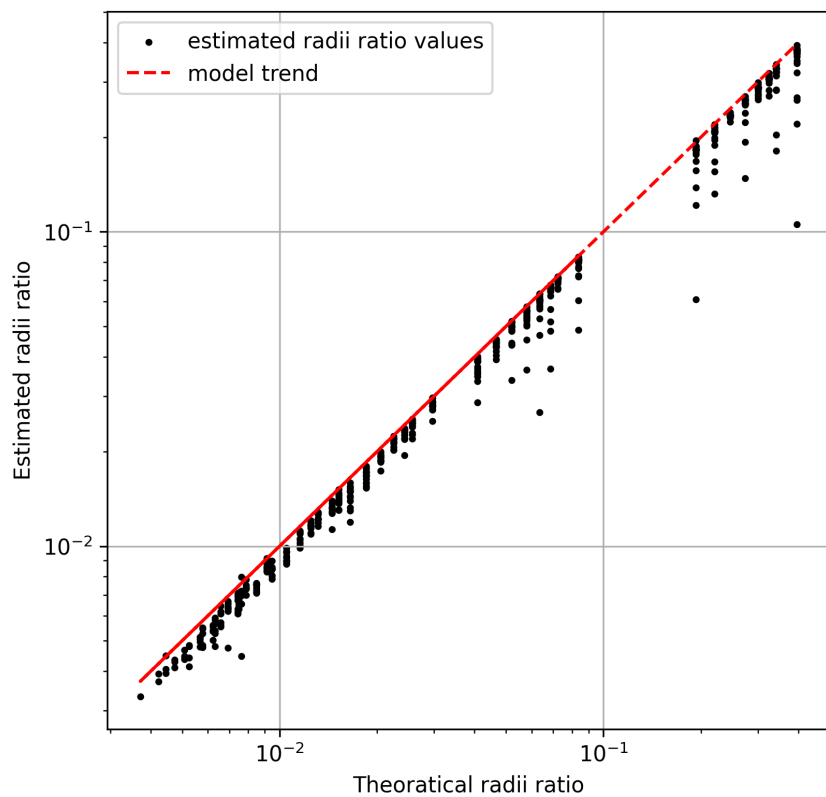


Figure 3.11: Radii ratio estimates of all the detected planetary systems (Black dots). The expected linear relation (red dashed line).

the system.

Next, we examine the errors associated with our estimate of radii ratios. The relative error as given in the equation (3.1) is visualized in the Figure 3.13.

$$\delta rp = \frac{rp_{\text{theoretical}} - rp_{\text{estimated}}}{rp_{\text{theoretical}}} \quad (3.1)$$

Where $rp_{\text{theoretical}}$ and $rp_{\text{estimated}}$ are theoretical and estimated values of radii ratios respectively. δrp is the relative error in the estimated radii ratios. We can see a significant drop in the errors with increasing radii ratio for 8.5 magnitude and this trend is similar until we reach the magnitude of 14.5 where we can note very irregular and scattered error values. For other magnitude bins, we can see higher error values for smaller radii ratios because the SNR is lower for smaller planets with an exponential decrease as we go to higher radii ratio values. Hence, PLATO promises remarkable accuracy in deduction of higher mass exoplanets up to the magnitude of 12.5. The inaccuracies in estimation of radii for smaller exoplanets for 8.5 magnitude go up to 18 percent but reduce significantly up to less than 5 percent with the increase in the exoplanet size. However, the estimates are still comparatively less accurate to simulations for Earth-like planets around Sun-like stars with induced stellar variability where the precision goes up to 3.6 percent ([Morris et al., 2020](#)).

3.3 Effect of SPR

As shown in Figure 2.3, after magnitude 16, the background/detector noise dominates over the photon noise making it unsuitable for planetary transit observations. The same has been demonstrated throughout this chapter with absolutely zero exoplanets less than the mass of Jupiter retrieved in the 16.5 magnitude bin. SPR which quantifies the amount of 3rd light that enters the aperture of the telescope proves to be a good indicator for the same. This is demonstrated in the Figure 3.14 where the mean SPR of all the configurations in a magnitude bin is plotted for all the magnitudes. The drastic increase in the SPR justifies the detection results observed in the entire chapter. The inaccuracies in the radii ratio value which is extensively seen for fainter targets are majorly a result of increasing noise and reducing SPR.

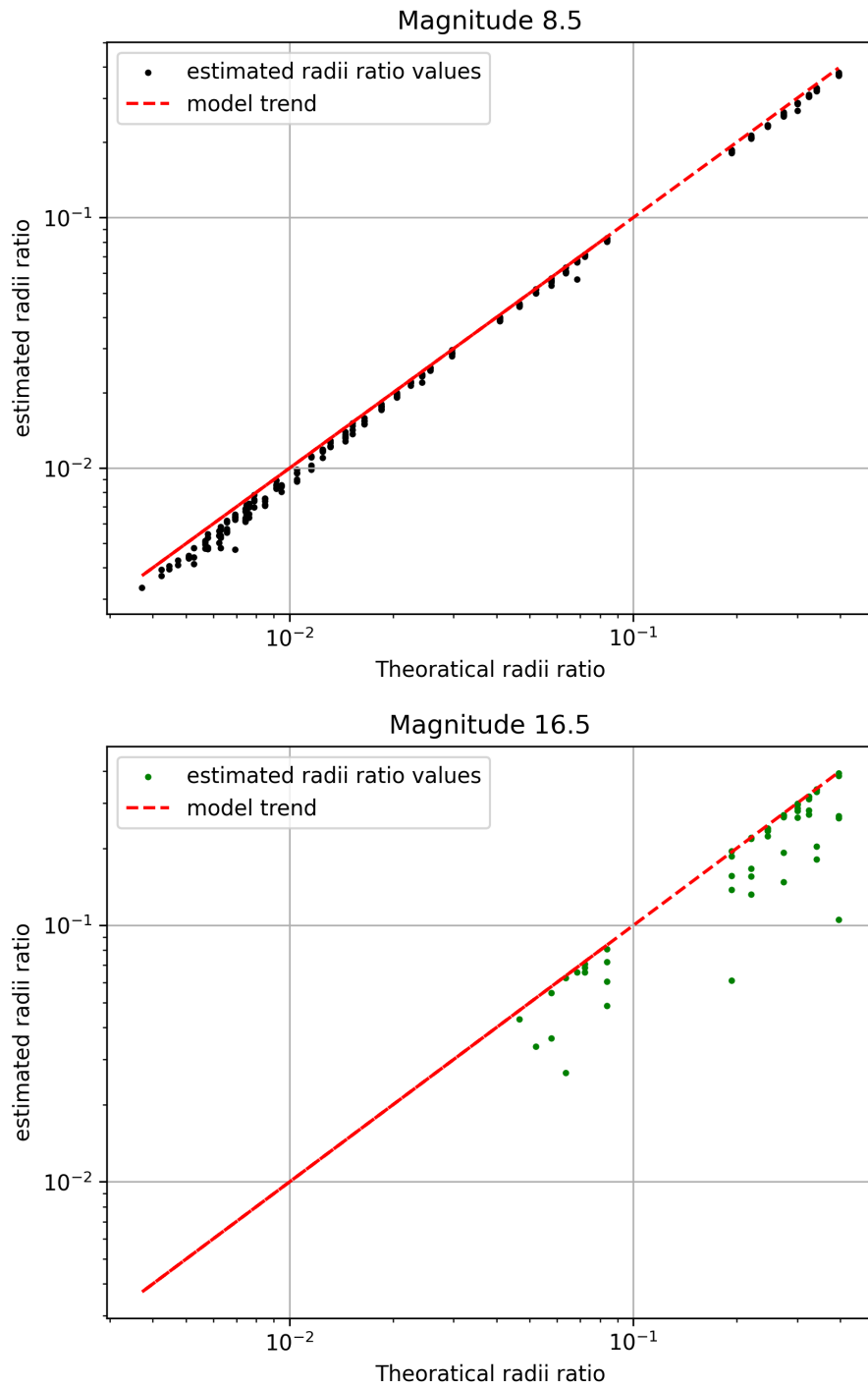


Figure 3.12: Radii ratio estimates plotted separately for 8.5 and 16.5 magnitude bins. The expected linear relation(red dashed line).

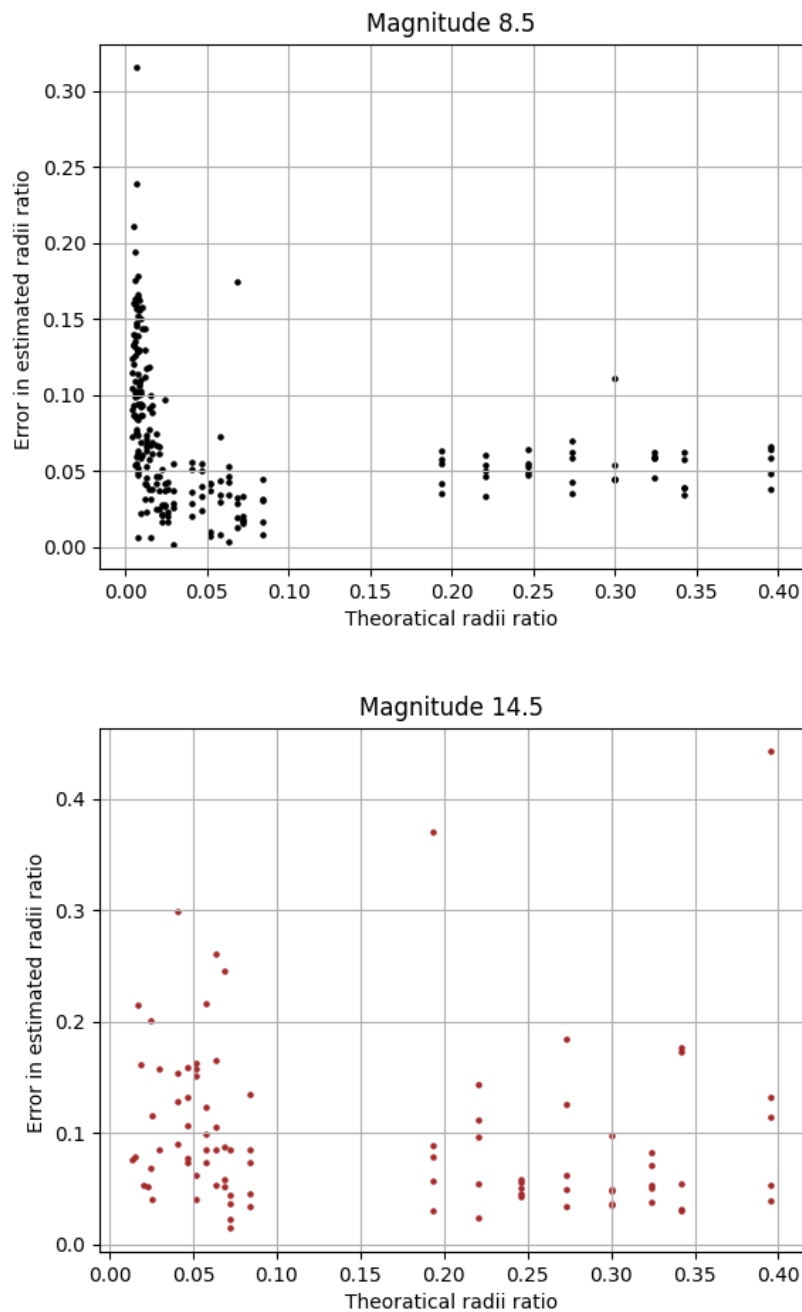


Figure 3.13: Errors in radii ratio estimates for 8.5 and 14.5 magnitude bins.

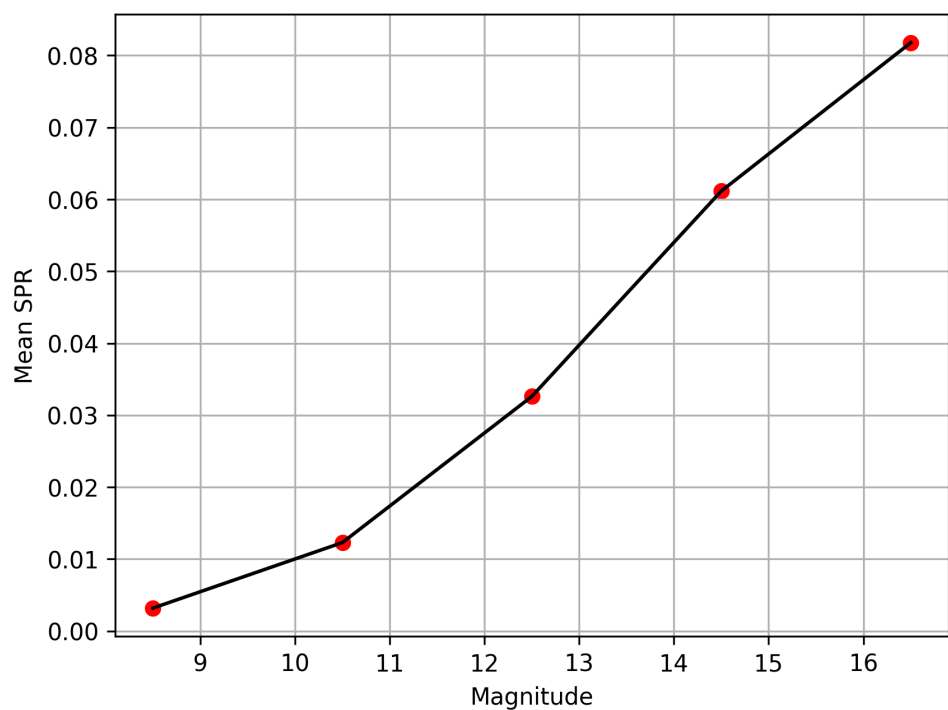


Figure 3.14: Mean SPR for all the magnitude bins

Chapter 4

Conclusions

This research has utilized the PlatoSim software to mimic expected data from PLATO and explore the telescope’s potential in detecting exoplanets in low SNR cases, putting its precision limits under a rigorous test. Scrutiny of such cases is necessary to understand PLATO’s efficiency in detecting exoplanets around stars more massive than the sun. The results indicated an excellent performance by PLATO in detecting exoplanets around intermediate stars of up to $2 M_{\odot}$ with high transit occurrence rates. Despite the inclusion of targets with very high magnitudes, the overall transit occurrence rates always exceed 55 percent for stars with masses less than $2 M_{\odot}$. The transit occurrence rates reach near unity for the $2 M_{\odot}$ cases if only the brightest targets are considered. For brighter targets, the transit occurrence rate was sufficiently good for stars more massive than $2 M_{\odot}$ as well. 90.8 and 71.25 percent exoplanets were retrieved around 8.5 and 10.5 magnitude systems respectively. This provides strong evidence for possibility of detection of transiting exoplanets around stars having mass ranges higher than the discoveries made through the current state of the art.

The research has demonstrated that PLATO is powerful enough in detecting transiting exoplanets having size more than or equal to Jupiter around stars as massive as early A/late B types. The estimation of radii ratios for bright targets has shown remarkable accuracy across the entire parameter space. The errors in radii ratio estimates followed the expected trend for brighter targets showing a decrease in error values with increasing radii ratio. This result builds up promising expectations for studies on exoplanet characterization with PLATO. The targets having spectral type between B9 to F5 are not included in the asPIC. This research proves to be a stepping stone in exploration of a broader parameter space for the mission with possible inclusion of intermediate-mass stars.

A common conclusion from all the results from this study indicates an outstanding performance of PLATO for transit detections around higher mass stars with low magnitude, emphasizing their inclusion as PLATO targets. However, the results presented in this research only take into account a very optimistic set of parameters and need more scrutiny for a more realistic detection statistic as will be discussed in the next section.

4.1 Future Outlook

Although the initial results from this research look promising in PLATO’s detection capabilities around intermediate-mass stars, there are still lots of parameters left to explore

before determining a definite catalog for the search of exoplanets around intermediate-mass stars that are within the observational boundary of the telescope. All the simulations carried out in the research consider the 24-camera region of the telescope as seen in Figure 1.6. The regions corresponding to 6, 12 and 18 cameras remain unexplored in this thesis. Simulating such cases is extremely critical in understanding the capabilities of PLATO in its entire FoV. As expected from the NSR studies, the SNR must drop with the reduced number of cameras that are focused on the target putting the PLATO's limit through a more severe investigation.

The presence of stellar variability is another estimate that can lead to extra contamination in the transit data making the process of transit retrieval more challenging. In such cases, the use of pre-whitening algorithms is required along with detrending methods to remove periodic signals corresponding to effects from the contamination. Additionally, post-main sequence stars in a similar mass range can be included in the parameter space for complete generalization of all the targets in the stellar neighborhood having a similar mass range. Stars when in their post main sequence phase, have comparatively higher radii compared to a main sequence star of the same mass. This makes it more challenging to find exoplanets around them due to drop in SNR.

Finally, the last required test before a definite set of targets can be shortlisted for PLATO for photometric extraction is to consider the actual population distribution of intermediate stars in the night sky. This will provide extra insights into the realistic transit occurrence rates of PLATO further shaping the way to create a sample of stars in the spectral range of B9 to F9. With the inclusion of the exoplanet search around intermediate-mass stars as a goal of the PLATO mission, a broader statistical study of exoplanetary systems will be accessible, consequently advancing our understanding of transiting exoplanets.

Bibliography

Baglin Annie, Team CoRoT, others . COROT: A minisat for pionnier science, asteroseismology and planets finding // Advances in Space Research. 2003. 31, 2. 345–349.

Börner Anko, Paproth Carsten, Cabrera Juan, Pertenaïs Martin, Rauer Heike, Mas-Hesse J Miguel, Pagano Isabella, Alvarez Jose Lorenzo, Erikson Anders, Grießbach Denis, others . PLATO's signal and noise budget // Experimental Astronomy. 2024. 58, 1. 1.

Borucki William, Koch David, Basri Gibor, Batalha Natalie, Brown Timothy, Caldwell Douglas, Christensen-Dalsgaard Jørgen, Cochran William, Dunham Edward, Gautier Thomas N, others . Finding Earth-size planets in the habitable zone: the Kepler Mission // Proceedings of the International Astronomical Union. 2007. 3, S249. 17–24.

Bundy Kevin A., Marcy Geoffrey W. A Search for Transit Effects in Spectra of 51 Pegasi and HD 209458 // Publications of the Astronomical Society of the Pacific. nov 2000. 112, 777. 1421.

Cenadelli Davide, Bernagozzi Andrea. The Discovery of the First Exoplanets // Handbook of Exoplanets. Cham: Springer International Publishing, 2018. 3–20.

Charbonneau David, Brown Timothy M., Latham David W., Mayor Michel. Detection of Planetary Transits Across a Sun-like Star // The Astrophysical Journal. dec 1999. 529, 1. L45.

Deeg Hans J., Alonso Roi. Transit Photometry as an Exoplanet Discovery Method // Handbook of Exoplanets. Cham: Springer International Publishing, 2018. 633–657.

Deeg Hans J., Belmonte Juan Antonio. Handbook of Exoplanets. 2018.

Gaudi B. Scott, Stassun Keivan G., Collins Karen A., Beatty Thomas G., Zhou George, Latham David W., Bieryla Allyson, Eastman Jason D., Siverd Robert J., Crepp Justin R., Gonzales Erica J., Stevens Daniel J., Buchhave Lars A., Pepper Joshua, Johnson Marshall C., Colon Knicole D., Jensen Eric L. N., Rodriguez Joseph E., Bozza Valerio, Novati Sebastiano Calchi, D'Ago Giuseppe, Dumont Mary T., Ellis Tyler, Gaillard Clement, Jang-Condell Hannah, Kasper David H., Fukui Akihiko, Gregorio Joao, Ito Ayaka, Kielkopf John F., Manner Mark, Matt Kyle, Narita Norio, Oberst Thomas E., Reed Phillip A., Scarpetta Gaetano, Stephens Denice C., Yeigh Rex R., Zambelli Roberto, Fulton B. J., Howard Andrew W., James David J., Penny Matthew, Bayliss Daniel, Curtis Ivan A., Depoy D. L., Esquerdo Gilbert A., Gould Andrew, Joner Michael D., Kuhn Rudolf B., Labadie-Bartz Jonathan, Lund Michael B., Marshall Jennifer L., McLeod Kim K., Pogge Richard W., Relles Howard, Stockdale

- Christopher, Tan T. G., Trueblood Mark, Trueblood Patricia.* A giant planet undergoing extreme-ultraviolet irradiation by its hot massive-star host // . VI 2017. 546, 7659. 514–518.
- Hippke Michael, David Trevor J., Mulders Gijs D., Heller René.* Wōtan: Comprehensive Time-series Detrending in Python // The Astronomical Journal. sep 2019. 158, 4. 143.
- Hippke Michael, Heller René.* Optimized transit detection algorithm to search for periodic transits of small planets // . Mar 2019. 623. A39.
- Howell Steve B.* The Grand Challenges of Exoplanets // Frontiers in Astronomy and Space Sciences. 2020. 7.
- Jannsen N., De Ridder, J. , Seynaeve, D. , Regibo, S. , Huygen, R. , Royer, P. , Paproth, C. , Grießbach, D. , Samadi, R. , Reese, D. R. , Pertenaïs, M. , Grolleau, E. , Heller, R. , Niemi, S. M. , Cabrera, J. , Börner, A. , Aigrain, S. , McCormac, J. , Verhoeve, P. , Astier, P. , Kutrowski, N. , Vandenbussche, B. , Tkachenko, A. , Aerts, C. .* PlatoSim: an end-to-end PLATO camera simulator for modelling high-precision space-based photometry // AA. 2024. 681. A18.
- Kovács, G. , Zucker, S. , Mazeh, T. .* A box-fitting algorithm in the search for periodic transits // AA. 2002. 391, 1. 369–377.
- Kreidberg Laura.* batman: BAsic Transit Model cAlculatioN in Python // Publications of the Astronomical Society of the Pacific. nov 2015. 127, 957. 1161.
- Latham David W., Andersen Johannes, Geary John C., Rodrigues Orlando, Stefanik Robert P.* A fiber feed for precise radial velocity work with the CfA echelle spectrographs. // Fiber Optics in Astronomy. 3. I 1988. 269–276. (Astronomical Society of the Pacific Conference Series).
- Lee Chien-Hsiu.* Exoplanets: Past, Present, and Future // Galaxies. 2018. 6, 2.
- Lightkurve Collaboration , Cardoso J. V. d. M., C. Hedges, Gully-Santiago M., Saunders N., M. Cody A., Barclay T., Hall O., Sagear S., Turtelboom E., Zhang J., Tzanidakis A., Mighell K., Coughlin J., Bell K., Berta-Thompson Z., Williams P., Dotson J., Barentsen G.* Lightkurve: Kepler and TESS time series analysis in Python. XII 2018.
- Lindegren, Lennart , Dravins, Dainis .* The fundamental definition of “radial velocity” // AA. 2003. 401, 3. 1185–1201.
- Mayor Michel, Queloz Didier.* A Jupiter-mass companion to a solar-type star // . XI 1995. 378, 6555. 355–359.
- Montalto, M. , Piotto, G. , Marrese, P. M. , Nascimbeni, V. , Prisinzano, L. , Granata, V. , Marinoni, S. , Desidera, S. , Ortolani, S. , Aerts, C. , Alei, E. , Altavilla, G. , Benatti, S. , Börner, A. , Cabrera, J. , Claudi, R. , Deleuil, M. , Fabrizio, M. , Gizon, L. , Goupil, M. J. , Heras, A. M. , Magrin, D. , Malavolta, L. , Mas-Hesse, J. M. , Pagano, I. , Paproth, C. , Pertenaïs, M. , Pollacco, D. , Ragazzoni, R. , Ramsay, G. , Rauer, H. , Udry, S. .* The all-sky PLATO input catalogue // AA. 2021. 653. A98.

Morris Brett M, Bobra Monica G, Agol Eric, Lee Yu Jin, Hawley Suzanne L. The stellar variability noise floor for transiting exoplanet photometry with PLATO // Monthly Notices of the Royal Astronomical Society. 03 2020. 493, 4. 5489–5498.

Mosteller Frederick, Tukey John W. Data analysis and regression. A second course in statistics // Addison-Wesley series in behavioral science: quantitative methods. 1977.

NASA Exoplanet Archive. 2024.

PLATO Defination study report. ESA's PLATO Defination study report. 2017.

Paxton Bill, Bildsten Lars, Dotter Aaron, Herwig Falk, Lesaffre Pierre, Timmes Frank. MODULES FOR EXPERIMENTS IN STELLAR ASTROPHYSICS (MESA) // The Astrophysical Journal Supplement Series. dec 2010. 192, 1. 3.

Pertenais Martin, Cabrera Juan, Paproth Carsten, Boerner Anko, Grießbach Denis, Mogulsky Valery, Rauer Heike. The unique field-of-view and focusing budgets of PLATO // International Conference on Space Optics — ICSO 2020. 11852. VI 2021. 118524Y. (Society of Photo-Optical Instrumentation Engineers (SPIE) Conference Series).

Pont Frédéric, Zucker Shay, Queloz Didier. The effect of red noise on planetary transit detection // . XI 2006. 373, 1. 231–242.

Rauer Heike, Heras Ana, Mas-Hesse Miguel, Pagano Isabella. PLATO Mission Overview // European Planetary Science Congress. IX 2024. EPSC2024-197.

Ricker George R, Winn Joshua N, Vanderspek Roland, Latham David W, Bakos Gáspár Á, Bean Jacob L, Berta-Thompson Zachory K, Brown Timothy M, Buchhave Lars, Butler Nathaniel R, others. Transiting exoplanet survey satellite // Journal of Astronomical Telescopes, Instruments, and Systems. 2015. 1, 1. 014003–014003.

Samadi R., Deru A., Reese, D., Marchiori, V., Grolleau, E., Green, J. J., Pertenais, M., Lebreton, Y., Deheuvels, S., Mosser, B., Belkacem, K., Börner, A., Smith, A. M. S. . The PLATO Solar-like Light-curve Simulator - A tool to generate realistic stellar light-curves with instrumental effects representative of the PLATO mission // AA. 2019. 624. A117.

Seager Sara. Exoplanets. 2011.

T. Prusti, Bruijne J. H. J. de, Brown A. G. A., Vallenari A., Babusiaux C., Bailer-Jones C. A. L., Bastian U., Biermann M., Evans D. W., Eyer L., Jansen F., Jordi C., Klioner S. A., Lammers U., Lindegren L., Luri X., Mignard F., Milligan D. J., Panem C., Poinsignon V., Pourbaix D., Randich S., Sarri G., Sartoretti P., Siddiqui H. I., Soubiran C., Valette V., Leeuwen F. van, Walton N. A., Aerts C., Arenou F., Cropper M., Drimmel R., Høg E., Katz D., Lattanzi M. G., O'Mullane W., Grebel E. K., Holland A. D., Huc C., Passot X., Bramante L., Cacciari C., Castañeda J., Chaoul L., Cheek N., De Angeli F., Fabricius C., Guerra R., Hernández J., Jean-Antoine-Piccolo A., Masana E., Messineo R., Mowlavi N., Nienartowicz K., Ordóñez-Blanco D., Panuzzo P., Portell J., Richards P. J., Riello M., Seabroke G. M., Tanga P., Thévenin F., Torra J., Els S. G., Gracia-Abril G., Comoretto G., Garcia-Reinaldos M., Lock T.,

Mercier E., Altmann M., Andrae R., Astraatmadja T. L., Bellas-Velidis I., Benson K., Berthier J., Blomme R., Busso G., Carry B., Cellino A., Clementini G., Cowell S., Creevey O., Cuypers J., Davidson M., De Ridder J., Torres A. de, Delchambre L., Dell'Oro A., Ducourant C., Frémat Y., García-Torres M., Gosset E., Halbwachs J.-L., Hambly N. C., Harrison D. L., Hauser M., Hestroffer D., Hodgkin S. T., Huckle H. E., Hutton A., Jasniewicz G., Jordan S., Kontizas M., Korn A. J., Lanzafame A. C., Manteiga M., Moitinho A., Muinonen K., Osinde J., Pancino E., Pauwels T., Petit J.-M., Recio-Blanco A., Robin A. C., Sarro L. M., Siopis C., Smith M., Smith K. W., Sozzetti A., Thuillot W., Reeven W. van, Viala Y., Abbas U., Abreu Aramburu A., Accart S., Aguado J. J., Allan P. M., Allasia W., Altavilla G., Álvarez M. A., Alves J., Anderson R. I., Andrei A. H., Anglada Varela E., Antiche E., Antoja T., Antón S., Arcay B., Atzei A., Ayache L., Bach N., Baker S. G., Balaguer-Núñez L., Barache C., Barata C., Barbier A., Barblan F., Baroni M., Navascués D. Barrado y, Barros M., Barstow M. A., Becciani U., Bellazzini M., Bellei G., Bello García A., Belokurov V., Bendjoya P., Berihuete A., Bianchi L., Bienaymé O., Billebaud F., Blagorodnova N., Blanco-Cuaresma S., Boch T., Bombrun A., Borrachero R., Bouquillon S., Bourda G., Bouy H., Bragaglia A., Breddels M. A., Brouillet N., Brüsemeister T., Bucciarelli B., Budnik F., Burgess P., Burgon R., Burlacu A., Busonero D., Buzzi R., Caffau E., Cambras J., Campbell H., Cancelliere R., Cantat-Gaudin T., Carlucci T., Carrasco J. M., Castellani M., Charlot P., Charnas J., Charvet P., Chassat F., Chiavassa A., Clotet M., Cocozza G., Collins R. S., Collins P., Costigan G., Criofa F., Cross N. J. G., Crosta M., Crowley C., Dafonte C., Damerdji Y., Dapergolas A., David P., David M., De Cat P., Felice F. de, Laverny P. de, De Luise F., De March R., Martino D. de, Souza R. de, Deboscher J., Pozo E. del, Delbo M., Delgado A., Delgado H. E., Marco F. di, Di Matteo P., Diakite S., Distefano E., Dolding C., Dos Anjos S., Drazinos P., Durán J., Dzigan Y., Ecale E., Edvardsson B., Enke H., Erdmann M., Escolar D., Espina M., Evans N. W., Eynard Bontemps G., Fabre C., Fabrizio M., Faigler S., Falcão A. J., Farràs Casas M., Faye F., Federici L., Fedorets G., Fernández-Hernández J., Fernique P., Fienga A., Figueras F., Filippi F., Findeisen K., Fonti A., Fouesneau M., Fraile E., Fraser M., Fuchs J., Furnell R., Gai M., Galleti S., Galluccio L., Garabato D., García-Sedano F., Garé P., Garofalo A., Garralda N., Gavras P., Gerssen J., Geyer R., Gilmore G., Girona S., Giuffrida G., Gomes M., González-Marcos A., González-Núñez J., González-Vidal J. J., Granvik M., Guerrier A., Guillout P., Guiraud J., Gúrpide A., Gutiérrez-Sánchez R., Guy L. P., Haigron R., Hatzidimitriou D., Haywood M., Heiter U., Helmi A., Hobbs D., Hofmann W., Holl B., Holland G., Hunt J. A. S., Hypki A., Icardi V., Irwin M., Fombelle G. Jevardat de, Jofré P., Jonker P. G., Jorissen A., Julbe F., Karampelas A., Kochoska A., Kohley R., Kolenberg K., Kontizas E., Koposov S. E., Kordopatis G., Kousky P., Kowalczyk A., Krone-Martins A., Kudryashova M., Kull I., Bachchan R. K., Lacoste-Seris F., Lanza A. F., Lavigne J.-B., Le Poncin-Lafitte C., Lebreton Y., Lebzelter T., Leccia S., Leclerc N., Lecoeur-Taibi I., Lemaitre V., Lenhardt H., Leroux F., Liao S., Licata E., Lindström H. E. P., Lister T. A., Livanou E., Lobel A., Löffler W., López M., Lopez-Lozano A., Lorenz D., Loureiro T., MacDonald I., Magalhães Fernandes T., Managau S., Mann R. G., Mantelet G., Marchal O., Marchant J. M., Marconi M., Marie J., Marinoni S., Marrese P. M., Marschalkó G., Marshall D. J., Martín-Fleitas J. M., Martino M., Mary N., Matijević G., Mazeh T., McMillan P. J., Messina S., Mestre A., Michalik D., Millar N. R., Miranda B. M. H., Molina D., Molinaro R., Molinaro M.,

Molnár L., Moniez M., Montegriffo P., Monteiro D., Mor R., Mora A., Morbidelli R., Morel T., Morgenthaler S., Morley T., Morris D., Mulone A. F., Muraveva T., Musella I., Narbonne J., Nelemans G., Nicastro L., Noval L., Ordénovic C., Ordieres-Meré J., Osborne P., Pagani C., Pagano I., Pailler F., Palacin H., Palaversa L., Parsons P., Paulsen T., Pecoraro M., Pedrosa R., Pentikäinen H., Pereira J., Pichon B., Piersimoni A. M., Pineau F.-X., Plachy E., Plum G., Poujoulet E., Prša A., Pulone L., Ragaini S., Rago S., Rambaux N., Ramos-Lerate M., Ranalli P., Rauw G., Read A., Regibo S., Renk F., Reylé C., Ribeiro R. A., Rimoldini L., Ripepi V., Riva A., Rixon G., Roelens M., Romero-Gómez M., Rowell N., Royer F., Rudolph A., Ruiz-Dern L., Sadowski G., Sagristà Sellés T., Sahlmann J., Salgado J., Salguero E., Sarasso M., Savietto H., Schnorhk A., Schultheis M., Sciacca E., Segol M., Segovia J. C., Segransan D., Serpell E., Shih I-C., Smareglia R., Smart R. L., Smith C., Solano E., Solitro F., Sordo R., Soria Nieto S., Souchay J., Spagna A., Spoto F., Stampa U., Steele I. A., Steidelmüller H., Stephenson C. A., Stoev H., Suess F. F., Süveges M., Surdej J., Szabados L., Szegedi-Elek E., Tapiador D., Taris F., Tauran G., Taylor M. B., Teixeira R., Terrett D., Tingley B., Trager S. C., Turon C., Ulla A., Utrilla E., Valentini G., Elteren A. van, Van Hemelryck E., Leeuwen M. van, Varadi M., Vecchiato A., Veljanoski J., Via T., Vicente D., Vogt S., Voss H., Votruba V., Voutsinas S., Walmsley G., Weiler M., Weingrill K., Werner D., Wevers T., Whitehead G., Wyrzykowski Ł., Yoldas A., Žerjal M., Zucker S., Zurbach C., Zwitter T., Alecu A., Allen M., Allende Prieto C., Amorim A., Anglada-Escudé G., Arsenijevic V., Azaz S., Balm P., Beck M., Bernstein H.-H., Bigot L., Bijaoui A., Blasco C., Bonfigli M., Bono G., Boudreault S., Bressan A., Brown S., Brunet P.-M., Bunclark P., Buonanno R., Butkevich A. G., Carret C., Carrion C., Chemin L., Chéreau F., Corcione L., Darmigny E., Boer K. S. de, Teodoro P. de, Zeeuw P. T. de, Delle Luche C., Domingues C. D., Dubath P., Fodor F., Frézouls B., Fries A., Fustes D., Fyfe D., Gallardo E., Gallegos J., Gardiol D., Gebran M., Gomboc A., Gómez A., Grux E., Gueguen A., Heyrovsky A., Hoar J., Iannicola G., Isasi Parache Y., Janotto A.-M., Joliet E., Jonckheere A., Keil R., Kim D.-W., Klagyivik P., Klar J., Knude J., Kochukhov O., Kolka I., Kos J., Kutka A., Lainey V., LeBouquin D., Liu C., Loreggia D., Makarov V. V., Marseille M. G., Martayan C., Martinez-Rubi O., Massart B., Meynadier F., Mignot S., Munari U., Nguyen A.-T., Nordlander T., Ocvirk P., O'Flaherty K. S., Olias Sanz A., Ortiz P., Osorio J., Oszkiewicz D., Ouzounis A., Palmer M., Park P., Pasquato E., Peltzer C., Peralta J., Péturaud F., Pieniluoma T., Pigozzi E., Poels J., Prat G., Prod'homme T., Raison F., Rebordao J. M., Risquez D., Rocca-Volmerange B., Rosen S., Ruiz-Fuertes M. I., Russo F., Sembay S., Serraller Vizcaino I., Short A., Siebert A., Silva H., Sinachopoulos D., Slezak E., Soffel M., Sosnowska D., Straižys V., Linden M. ter, Terrell D., Theil S., Tiede C., Troisi L., Tsalmantza P., Tur D., Vaccari M., Vachier F., Valles P., Van Hamme W., Veltz L., Virtanen J., Wallut J.-M., Wichmann R., Wilkinson M. I., Ziaeepour H., Zschocke S. The Gaia mission // Astronomy amp; Astrophysics. XI 2016. 595. A1.

Winn Joshua N. Exoplanet transits and occultations. 55. 2010.

Winn Joshua N. The Transiting Exoplanet Survey Satellite. 2024.

Wolszczan A., Frail D. A. A planetary system around the millisecond pulsar PSR1257 + 12 // . I 1992. 355, 6356. 145–147.

Wright Jason T., Gaudi B. Scott. Exoplanet Detection Methods // Planets, Stars and Stellar Systems. Volume 3: Solar and Stellar Planetary Systems. 2013. 489.

Zhou Yifan, Herczeg Gregory J., Kraus Adam L., Metchev Stanimir, Cruz Kelle L. Accretion onto Planetary Mass Companions of Low-mass Young Stars // . III 2014. 783, 1. L17.

Appendices

Appendix A

Appendix

The following hyperlink will lead to a github page containing the entire parameter space, input and output data from PlatoSim, transit retrieval procedure, and detection analysis. It also contains some relevant figures from the entire project: [Thesis Appendix github link](#)

AFDELING
Straat nr bus 0000
3000 LEUVEN, BELGIË
tel. + 32 16 00 00 00
fax + 32 16 00 00 00
www.kuleuven.be

